The $\beta2^{V287L}$ nicotinic subunit linked to sleep-related epilepsy differently affects fast-spiking and regular spiking somatostatin-expressing neurons in murine prefrontal cortex.

Simone Meneghini[1], Debora Modena[2], Giulia Colombo[1], Aurora Coatti[1], Niccolò Milani[2],

Laura Madaschi[3], Alida Amadeo[2], and Andrea Becchetti[1*]

[1]Department of Biotechnology and Biosciences, University of Milano-Bicocca and NeuroMI,

Milan Center of Neuroscience, 20126 Milan, Italy.

[2]Department of Biosciences, University of Milano, 20133 Milan, Italy.

[3] UNITECH NOLIMITS, University of Milano, Via Celoria 26, 20133 Milan, Italy.

*Correspondence to:

Andrea Becchetti, Department of Biotechnology and Biosciences, University of Milano-Bicocca, piazza della Scienza 2, 20126 Milan, Italy;

Tel.: +39-02-64483301; E-mail: andrea.becchetti@unimib.it

ABSTRACT

Mutant subunits of the neuronal nicotinic ACh receptor (nAChR) can cause Autosomal Dominant Sleep-related Hypermotor Epilepsy (ADSHE), characterized by frontal seizures during non-rapid eye movement (NREM) sleep. We studied the cellular bases of the pathogenesis in brain slices from mice conditionally expressing the ADSHE-linked $\beta2^{V287L}$ nAChR subunit. $\beta2^{V287L}$ mice displayed minor structural alterations, except for a ~10% decrease of prefrontal cortex thickness. However, they showed a substantial decrease of the excitatory input to layer V fast-spiking (FS) interneurons, despite a concomitant increase in the number of glutamatergic terminals around the cell soma. Hence, prefrontal hyperexcitability may depend on a permanent impairment of surround inhibition. The effect disappeared when $\beta2^{V287L}$ was silenced until postnatal day 15th, suggesting that the transgene selectively affects the maturation of glutamatergic synapses on FS neurons. The other main population of interneurons in layer V was constituted by somatostatin-expressing regular spiking cells. When tested with 10 μM nicotine, these displayed larger somatic nicotinic currents in transgenic mice. Thus, during wakefulness, activation of $\beta2^{V287L}$-containing nAChRs by the high cholinergic tone may counteract hyperexcitability by promoting local inhibition by somatostatin-expressing cells and decreasing the effect of glutamatergic deficit in FS neurons. This interpretation was tested in networks disinhibited by 2 μM bicuculline. Slices expressing $\beta2^{V287L}$ were more susceptible to develop synchronized activity in the absence of nicotine. Addition of the drug boosted excitability in the controls, but had little effect in $\beta2^{V287L}$. Our findings suggest why NREM sleep favors ADSHE seizures and nicotine can be palliative in patients.

ABBREVIATIONS

ACSF, artificial cerebro-spinal fluid; (AD)SHE, (autosomal dominant) sleep-related hypermotor epilepsy; AP, action potential; AP-5, D(-)-2-amino-5-phosphono-pentanoic acid; ChAT, choline acetyltransferase; CNQX, 6-cyano-7-nitroquinoxaline-2,3-dione; DHβE, dihydro-β-erythroidine; EEG, electroencephalography; E_{Cl}, equilibrium potential for Cl$^-$; E_{GABA}, reversal potential for GABA$_A$ currents; EPSC, excitatory post-synaptic current; EPSP, excitatory postsynaptic potential; Fr2, frontal area 2; FS, fast-spiking; GAD67, glutamic acid decarboxylase 67; IPSC, inhibitory post-synaptic current; LDT, laterodorsal tegmental nucleus; NBM, nucleus basalis magnocellularis; nAChR, nicotinic acetylcholine receptor; NREM, non-rapid eye movement; PFC, prefrontal cortex; PPT, pedunculopontine nucleus; PV, parvalbumin; ROI, region of interest; RSNP, regular spiking non pyramidal; RT, room temperature; SOM, somatostatin; SS, somatosensory cortex; SYN, synaptophysin; tTA, tetracycline-controlled transcriptional activator; TTX, tetrodotoxin; VAChT, vesicular ACh transporter; VGAT, vesicular GABA transporter; VGLUT1, vesicular glutamate transporter 1; V_m, membrane potential; V_{rest}, resting membrane potential.

1. INTRODUCTION

ACh potently regulates excitability and arousal in the adult cerebral cortex by activating metabotropic (muscarinic) and ionotropic (nicotinic; nAChRs) receptors (Picciotto et al., 2012). Nicotinic receptors are pentameric cation channels formed by different combinations of α and β subunits, whose specific functions are debated. In the neocortex, nAChRs are mainly constituted by 1) the low-affinity homomeric $(\alpha 7)_5$, characterized by quick desensitization and a high permeability to Ca^{2+} (P_{Ca}), and 2) the high-affinity heteromeric β2-containing (β2*) receptors, with slower kinetics and lower P_{Ca} (Dani and Bertrand, 2007). The latter, and especially the widespread α4β2*, are major modulators of cortical circuits (Fonck et al., 2005; Couey et al., 2007; Bailey et al., 2010; Parikh et al., 2010; Guillem et al., 2011).

That α4β2*nAChRs have a lead role in neocortex excitability agrees with the observation that mutant *CHRNA4* and *CHRNB2* genes, respectively coding for the α4 and β2 nAChR subunits, are linked to Autosomal Dominant Sleep-related Hypermotor Epilepsy (ADSHE, formerly known as Autosomal Dominant Nocturnal Frontal Lobe Epilepsy; Steinlein et al., 1995; De Fusco et al., 2000; Phillips et al., 2001; Tinuper et al., 2016). ADSHE is the Mendelian form of SHE, a focal epilepsy whose hallmark is the abrupt occurrence of seizures during non-rapid eye movement (NREM) sleep. Seizure semiology is heterogeneous, but generally comprises clusters of hyperkinetic seizures arising in the frontal lobe (~70 % of the cases), or other neocortex regions (Tinuper et al., 2016; Gibbs et al., 2018).

A widely studied ADSHE mutation is $\beta 2^{V287L}$, which in heterologous expression systems causes a 'gain of function' phenotype by retarding α4β2 nAChR desensitization (De Fusco et al., 2000) and increasing its sensitivity to the agonists (Son et al., 2009; Nichols et al., 2016; Indurthi et al., 2019). This is a common feature of ADSHE mutations falling on either *CHRNA4* or *CHRNB2* (Dani and Bertrand, 2007; Becchetti et al., 2015), and may be a major component of the pathogenetic mechanism. Yet, the pathophysiological interpretation of *in*

vitro observations remains uncertain, because of the bewildering intricacy of the nAChR roles in the brain. These receptors regulate both excitatory and inhibitory transmission at the pre-, post- and extra-synaptic level, with a complex pattern that depends on brain region and cortical layer (Picciotto et al., 2012; Becchetti et al., 2015). A further complication is that nAChRs are implicated in cortical development and synaptogenesis (Bruel-Jungerman et al., 2011), and β2* nAChRs regulate synaptic maturation during the first postnatal weeks (Rossi et al., 2001; McLaughlin et al., 2003; Bailey et al., 2012; Lozada et al., 2012; Molas and Dierssen, 2014). Therefore, the functional alterations underlying ADSHE phenotype may comprise moment-to-moment effects of the mutant nAChRs on adult frontal circuit excitability as well as a permanent synaptic unbalance arisen during late developmental stages.

To better understand ADSHE pathogenesis, several mutant subunits have been expressed in rodent strains (Klaassen et al., 2006; Teper et al., 2007; Zhu et al., 2008; Manfredi et al., 2009; Xu et al., 2011; Shiba et al., 2015; Fukuyama et al., 2020). In knock-in mice, β2^{V287L} causes imbalance of the normal activity-rest circadian pattern (Xu et al., 2011), but spontaneous seizures are rare (O'Neill et al., 2013). In rats, β2^{V286L} (corresponding to the human β2^{V287L}) causes spontaneous paroxysmal arousal seizures during the light period (the murine resting/sleeping phase; Shiba et al., 2015). Even closer to the human pathology is the phenotype displayed by a transgenic murine strain conditionally expressing β2^{V287L} in a TET-off system (Manfredi et al., 2009). Mice expressing the transgene display brief spontaneous seizures (~25 s) during periods of increased EEG delta wave activity, which is typical of slow-wave sleep. Seizures are absent if the transgene is silenced during brain development, until the end of the second postnatal week, even if expression is subsequently reactivated. Hence, irreversible synaptic alterations may be caused by early action of β2^{V287L} (Manfredi et al., 2009).

Here, we use Manfredi's strain to map the synaptic alterations produced by β2^{V287L} on the dorsomedial prefrontal cortex (PFC), also known as frontal area 2 (Fr2), or secondary motor area (M2). This is a wide prefrontal associative area which projects to the motor cortex and

5

dorsolateral striatum and receives input from sensory and parietal cortices as well as dopamine neurons of the ventral tegmentum (Barthas and Kwan, 2017; Kawaguchi, 2017). Fr2 is thought to be implicated in the behavioral responses to situations that require immediate attention, thus being a major target of cholinergic action in PFC. Because of its pattern of connections, it could be directly implicated in generating hypermotor seizures and releasing the stereotyped motor patterns typically observed in SHE (Becchetti et al., 2015).

The cellular basis of seizure propensity in mice carrying $\beta 2^{V287L}$ were investigated in layer V, which is particularly susceptible to generate and spread epileptiform activity (Telfeian and Connors, 1998) and is a sensitive cholinergic target (Metherate et al., 1992). We analyzed pyramidal cells and the GABAergic interneuron populations more directly involved in controlling the spread of epileptiform activity in vitro, namely fast-spiking (FS) and regular spiking somatostatin (SOM)-expressing neurons (Trevelyan et al., 2006; Cammarota et al., 2013; Parrish et al., 2019). Synaptic and excitability features were studied in presence and absence of nAChR stimulation, to clarify the somewhat paradoxical observation that 'gain of function' nAChR mutations facilitate seizures during NREM sleep, i.e. when the cholinergic tone is lowest (Jones, 2020). Our study is also relevant to understand why nicotine treatment controls seizures in a fraction of human ADSHE patients (Becchetti et al., 2020).

2. MATERIAL AND METHODS

2.1. Animals

Mice were kept in pathogen-free conditions, with a 12 h light-dark cycle, and water and food *ad libitum*. Animal handling and experimentation comply with the Italian law (2014/26, which implemented the 2010/63/UE) and were approved by the Animal Welfare Ethical Committee of Milano-Bicocca University and by the Italian Ministry of Health (101/2016-PR). We used the S3 line of double transgenic FVB-TG (tTA:Chrnb2V287L) strain, which expresses the $\beta2^{V287L}$ nAChR subunit in the brain, under the tetracycline-controlled transcriptional activator (tTA; TET-off system). When necessary, the transgene was silenced by adding doxycycline to drinking water (1 mg/ml, with sucrose to mask the bitter taste). Genotyping was carried out following Manfredi et al. (2009). The double transgenic mice (hereafter $\beta2^{V287L}$) were compared with their littermates not expressing the transgene (Control), i.e. mice expressing the transactivator (tTA) or wild-type (WT), as indicated. We used mice of either sex between the 1st and the 4th postnatal month, as detailed in Results. No evidence was found of a sex-dependent effect on synaptic transmission. For example, in a representative group of litters (2nd and 3rd postnatal month), the frequency of spontaneous excitatory postsynaptic currents (EPSCs) in FS cells of control (tTA) mice was 37.2 ± 2.9 Hz (n = 8 ♀) and 39.1 ± 2.5 Hz (n = 9 ♂; NS with unpaired t-test); in $\beta2^{V287L}$ mice, EPSC frequency was 25 ± 2.4 Hz (n = 10 ♀), and 21.4 ± 2.2 Hz (n = 15 ♂; NS with unpaired t-test).

2.2. Tissue preparation and brain regions

For patch-clamp experiments, mice were sacrificed after isoflurane anesthesia. Brains were extracted by standard procedures and kept in ice-refrigerated solution containing (mM): 87 NaCl, 21 NaHCO$_3$, 1.25 NaH$_2$PO$_4$, 7 MgCl$_2$, 0.5 CaCl$_2$, 2.5 KCl, 25 D-glucose, 75 sucrose, and equilibrated with 95% O$_2$ and 5% CO$_2$ (pH 7.4), supplemented with ascorbic acid (79.2

mg/l). Coronal slices (300 μm thick) were cut between +2.58 and +2.10 mm from bregma, essentially comprising the region referred to as FrA in Franklin and Paxinos (2008), and the most anterior part of M2. For consistency with previous work and the nomenclature in rat, we will use Fr2 hereafter (for discussion, see Aracri et al., 2010). Slices were incubated in the above solution (1 h at room temperature, RT), before being transferred to the recording chamber.

For immunohistochemistry, mice were deeply anesthetized by intraperitoneal 4% chloral hydrate (2 ml/100 g), after isoflurane pre-anesthesia, and sacrificed by intracardiac perfusion as described (Aracri et al., 2013). Extracted brains were immersed in 4% paraformaldehyde in phosphate buffer (PB) for 24 h, at 4°C. By PFC, we refer to the wide dorsomedial shoulder of prefrontal cortex, including FrA and M2 (Franklin and Paxinos, 2008). Thus, coronal PFC sections (50 μm thick) were cut with a VT1000S vibratome (Leica Microsystems) between +2.58 and -0.06 mm from bregma. For somatosensory cortex (SS), we sampled the extended SS region between +1.54 and -1.64 mm from bregma. Stereological cell counts of cholinergic neurons were carried out on coronal brain sections between -5.02 and -4.36 mm from bregma, for pedunculopontine (PPT) and laterodorsal tegmental (LDT) nuclei, and between -0.34 and -0.82 mm from bregma for nucleus basalis magnocellularis (NBM). Anatomical coordinates are summarized in **Table 1**.

2.3. Primary antibodies

Anti-nAChR β2 subunit (anti-β2 nAChR): polyclonal, made in rabbit against the C-terminal 493-502 amino acids (Immunological Sciences; 1:200). Anti-synaptophysin (anti-SYN): monoclonal, made in mouse against human protein (Dako; 1:100). Anti-choline acetyl-transferase (anti-ChAT): polyclonal, made in goat against human placental enzyme (Millipore; 1:50). Anti-vesicular ACh transporter (anti-VAChT): polyclonal, made in goat against the C-terminal 475-530 amino acids of rat protein (Millipore; 1:300). Anti-parvalbumin (anti-PV; only for immunoperoxidase histochemistry): polyclonal, made in rabbit against the rat muscular

PV (SWant Inc.; 1:2000). Anti-PV (for immunofluorescence): monoclonal, made in mouse against the carp muscle protein (Sigma-Aldrich; 1:500). Anti-somatostatin (anti-SOM): monoclonal, made in mouse against the amino acids 25-116 of human SOM (Santa Cruz; 1:200). Anti-vesicular GABA transporter (anti-VGAT): polyclonal, made in rabbit against the synthetic peptide corresponding to the N-terminal 75-87 amino acids of the rat protein (Synaptic Systems; 1:800). Anti-GABA$_A$ α1 subunit: polyclonal, made in rabbit against the synthetic peptide corresponding to the 28-43 amino acids (Sigma: 1:300). Anti-glutamic acid decarboxylase 67 (anti-GAD67): polyclonal, made in goat against the human recombinant GAD67 type 1, rhGAD1 (aa 2-97) derived from *E. coli* (R&D Systems; 1:300). Anti-vesicular glutamate transporter 1 (anti-VGLUT1): polyclonal, made in rabbit against Strep-TagR-fusion proteins containing the amino acid residues 456-560 of the rat VGLUT1/BNPI (brain-specific Na1-dependent inorganic phosphate transporter; Synaptic Systems; 1:500).

2.4. Immunofluorescence histochemistry, colocalization and densitometric analysis, cell counting

Immunoreaction was carried out as reported (Amadeo et al., 2018). Sections were incubated for two nights with one to three primary antibodies. Hoechst (Molecular Probes) or NeuroTrace™ (Molecular Probes; 1:50) staining was applied for cytoarchitecture analysis and cell counting. After rinsing with phosphate buffered saline (PBS), sections were incubated with different mixtures of the following secondary fluorescent antibodies (75 min, RT): Alexa Fluor™488 or CF™488A-conjugated donkey anti-rabbit IgG (Invitrogen and Biotium, respectively; 1:200), CF™568-conjugated donkey anti-mouse (Sigma; 1:200); Alexa Fluor™488-conjugated donkey anti-goat (Invitrogen; 1:200). For anti-SOM and anti-β2 nAChR, biotinylated horse anti-mouse and biotinylated goat anti-rabbit (Vector Laboratories) were respectively used (75 min, RT), followed by PBS rinsing and CF™568-conjugated or Alexa Fluor™488-conjugated streptavidin incubation (2 h, RT). Finally, samples were rinsed

9

and mounted on coverslips (if necessary, after Hoechst staining), with PBS/glycerol (1:1 v/v) or Vectashield^{TM} (Vector Laboratories), and inspected with laser scanning confocal microscope, to visualize double or triple fluorescent labeling. Reaction specificity was assessed by negative controls (i.e., omission of primary antibodies).

Confocal micrographs were generally collected at 40× with a Leica SP2 or Nikon A1 laser scanning confocal microscope, except in the case of VAChT densitometric analysis and manual counting of PV+ or SOM+ cells on the same immunofluorescent sections. In this case, four confocal image stacks (total thickness 6 μm, seven optical planes) were acquired at 20× from different PFC sections of each animal. Densitometric analysis and manual cell counting were carried out with ImageJ software (NIH). Identical acquisition parameters were used for the same antigen, as previously described (Aracri et al., 2013). Briefly, non-overlapping pictures were acquired in at least two different neocortex sections per animal, so that double immunolabeling was studied in 3 or 4 fields per region in each animal. For densitometric analysis, 3 or 4 distinct images of cortical layers stained with nuclear counterstaining were acquired to sample the different areas. For each animal, the mean fluorescence intensity of each image was sometimes divided by the number of counted neurons therein, depending on the antigen distribution (somatodendritic or synaptic). The degree of colocalization of different markers was calculated by comparing the Manders' coefficients, calculated with the JACoP plug-in of ImageJ (Bolte and Cordeliéres, 2006).

2.5. Immunoperoxidase histochemistry and densitometric analysis

Sections were permeabilized and blocked following Aracri et al. (2018). Images from infra- or supragranular layers were magnified (10×), acquired with a slide scanner (Nanozoomer S60, Hamamatsu) and stored with NDPview2 software (Hamamatsu). Two different regions of interest (ROI) were designed on ImageJ for PFC and SS. For each animal, at least three different images for each cortical layer (II/III and V) from both PFC and SS (right and left hemisphere)

were acquired and analyzed. Each image was deconvolved and spatially calibrated with ImageJ, and a mean signal intensity (optical density) was obtained from the ROI pixels.

2.6. Cortical thickness and cell count by stereological method

Cortical thickness was measured on PFC and SS sections stained with thionin. PFC sections at P60 and P90 were cut every 350 μm between +1.98 mm and -0.22 mm from bregma. SS sections were cut every 750 μm, between +1.98 and -1.82 mm from bregma. For each genotype and cortical region, 30 measurements of thickness were carried out by using the Q-Capture Pro 7 software (QImaging, Inc.) and averaged. A similar rostro-caudal extension was investigated for the smaller P9 and P12. Neurons were counted at P60 by applying the Unbiased Optical Fractionator Stereology method, using the Optical Dissector workflow of StereoInvestigator 11 software (MicroBrightField Inc, Colchester, VT), on thionin-stained sections equally distant from each other and spanning the entire volume of the target area (Moroni et al., 2018). An analogous procedure was applied to count ChAT+ cells in cholinergic nuclei and PV+ neurons in neocortex. Because of the unreliable discrimination of cell bodies with anti-SOM antibody by immunoperoxidase method, SOM+ cells were only counted by immunofluorescence (see *2.4*). Brain areas were identified as stated in 2.2 (**Table 1**). For PFC, we selected 7 sections spaced 350 μm apart. ROIs were defined by inspection at 4× or 2.5× magnification. The workflow applies a grid on the ROI, which is then divided into smaller equally distant areas (counting frames or dissectors), in which cell bodies were counted randomly and systematically at 40× magnification. Cell counts were applied to the entire ROI volume, by coupling the XY scan with a Z scan.

2.7. 3D reconstruction and quantification of GABAergic cell types and synaptic terminals

Double and triple immunofluorescence images were analyzed with ArivisVision4D software (Arivis AG, Munich, Germany), to obtain 3D reconstruction of cells, neurites and

synapses. The number of contacts between cholinergic (VAChT+), glutamatergic (VGLUT1+), or GABAergic (VGAT+) synaptic terminals and SOM+ or PV+ cell bodies was analyzed on at least 20 neurons per animal. Images were acquired on the entire cell thickness with a Nikon A1 confocal microscope at 60× (1.6 zoom) on PFC layer V. After spatial calibration of the acquired images, for identification and reconstruction of VAChT+, VGLUT1+ and VGAT+ terminals we availed of the 'Blob finder' tool. After setting a signal intensity threshold and an object diameter appropriate to the staining (average size 800 nm), the software identifies the majority of individual objects (probability threshold was set to 1%, to consider the majority of the potential objects). The "Split sensitivity", the value that controls whether touching objects should be separated or merged, was set to 89,1%, ensuring appropriate segmentation of the small synaptic terminals. Cell bodies were identified and drawn on each optical plane. After segmentation, a different pipeline ('Segment colocalization') was created, which allowed to count the synaptic terminals contacting either SOM+ or PV+ somata. Only the synaptic terminals directly intersecting, contacting or residing inside the contour of the cell bodies (within a distance of one voxel) were considered.

2.8. Dendritic arborization and spine density

We used the Golgi-Cox method to stain 300 μm thick slices from PFC (2.58 -1.14 mm from bregma) of 4 WT (2 ♀ and 2 ♂) and 4 β2^{V287L} (3 ♀ and 1 ♂; all aged > P60). Sections were imaged by acquiring z-stacks with an Eclipse Ti2 confocal microscope (Nikon) at 40× magnification and 2048-pixel resolution. Analysis was carried out with Fiji ImageJ (Simple Neurite Tracer and Cell Count plugins). From 4 to 17 pyramidal neurons per cortical layer were considered in each mouse. Dendritic arbor complexity was quantified by Sholl analysis (Sholl, 1953) on z-stacks of pyramidal neurons having the most part of basal dendrites spared by the slice cut. The number of intersections were counted between dendrites and 10 μm-spaced concentric spherical surfaces centered on the soma. The ramification index was calculated by

dividing the maximal N of dendrites by the number of primary dendrites. Dendritic spines were counted every 10 μm on at least three dendrites per cell. The mean values for each cell were plotted against dendrite length to assess the spines' distribution.

2.9. Chemicals and drugs for electrophysiology

Chemicals were purchased from Sigma-Aldrich, except D(-)-2-amino-5-phosphono-pentanoic acid (AP-5), 6-cyano-7-nitroquinoxaline-2,3-dione (CNQX), and tetrodotoxin (TTX), which were purchased by Tocris Bioscience (Bristol, UK). Stock solutions of (−)-nicotine hydrogen tartrate salt, dihydro-β-erythroidine hydrobromide (DHβE), (−)-bicuculline methiodide, AP-5, 5-HT and TTX were prepared in distilled water and stored at -20°C. CNQX was dissolved in dimethylsulfoxide. Stock solutions were diluted daily in artificial cerebrospinal fluid (ACSF).

2.10. Whole-cell patch-clamp recordings in acute brain slices

Cells were examined with an Eclipse E600FN microscope with water immersion DIC objective (Nikon), equipped with IR digital CCD C8484-05G01 camera and HCImage Live acquisition software (Hamamatsu Photonics). Neurons were voltage- or current-clamped with a Multiclamp 700A amplifier (Molecular Devices), at 33-34°C. Borosilicate capillaries (Corning) were pulled with a P-97 Flaming/Brown Micropipette Puller (Sutter Instruments) to a final resistance of 2-3 MΩ. The cell capacitance and series resistance (up to ~75%) were always compensated. Experimental traces were low-pass filtered at 2 kHz and digitized at 10 kHz, with pClamp9/Digidata 1322A (Molecular Devices). For display, they were sometimes further low-pass filtered at ~300 Hz. Slices were perfused at ~2 ml/min with ACSF (mM): 129 NaCl, 21 NaHCO$_3$, 1.6 CaCl$_2$, 3 KCl, 1.25 NaH$_2$PO$_4$, 1.8 MgSO$_4$, 10 D-glucose, aerated with 95% O$_2$ and 5% CO$_2$ (pH 7.4). For EPSC recording and action potential (AP) profiling, pipette contained (mM): 135 K-gluconate, 5 KCl, 1 MgCl$_2$, 2 MgATP, 0.3 Na$_2$GTP, 0.5 BAPTA, 10

HEPES (pH 7.25-7.3, adjusted with KOH). To record inhibitory post-synaptic currents (IPSCs) from pyramidal neurons, pipette contained (mM): 140 Cs-gluconate, 1 $MgCl_2$, 2 MgATP, 0.3 Na_2GTP, 0.5 BAPTA, 10 HEPES (pH 7.25-7.3). By blocking K^+ currents with Cs^+, IPSCs could be recorded as outward currents around the reversal potential of glutamatergic currents (0/+10 mV), thus avoiding application of glutamate receptors' blockers. This method cannot be applied to GABAergic cell populations, which cannot be easily identified by morphology. In this case, pipette contained (mM): 70 K-gluconate, 70 KCl, 1 $MgCl_2$, 2 MgATP, 0.3 Na_2GTP, 0.5 BAPTA, 10 HEPES (pH 7.25-7.3). In these conditions, E_{Cl} was approximately -17 mV, and IPSCs were measured as inward currents at -70 mV, while EPSCs were inhibited by AP-5 (10 µM) and CNQX (40 µM). No correction for liquid junction potentials was applied to the V_m values reported in the text. Input resistance was measured by applying small stimuli around V_{rest} and was constantly monitored during the experiment. It was usually around 100 MΩ for pyramidal and RSNP neurons and 50-60 MΩ for FS cells in the second postnatal month. Drugs were applied in the bath and their effect usually reached the steady state within 2 min. EPSCs and IPSCs were registered for 2 to 5 min after obtaining the whole-cell configuration. When needed, 10 µM nicotine was applied for 5 min. Only one cell was treated per slice, to avoid long-term nAChR inactivation. The synaptic events' frequency after washout was generally higher than 70% of the initial value. Cells in which this value was lesser than 50% were discarded. Focal application of 5-HT was obtained by ejection through a glass micropipette connected to a pneumatic IM-11-2 microinjector (Narishige, Japan).

2.11. Analysis of synaptic events and APs

Analysis was carried out with Clampfit 9.2 (Molecular Devices), OriginPro 2018 (OriginLab Corporation), and Mini Analysis (Synaptosoft Inc.). Spike amplitude was calculated as the difference between AP threshold and peak. Spike width was calculated at half-amplitude. Adaptation was measured at a mean firing frequency of ~100 Hz. After-hyperpolarization

(AHP) was computed as the difference between spike threshold and the most negative V_m reached after repolarization. Synaptic events were analyzed one by one within segments of continuous recording (2 min), at the beginning of experiment (for basal synaptic events), or immediately before and after applying nicotine. The analyzed time segments usually included hundreds (often thousands) of synaptic events. The baseline noise was generally < 5 pA (peak-to-peak). For both EPSCs and IPSCs, the detection threshold was set at 6-7 pA, as the minimal amplitude of synaptic events is expected to be around 5 pA (e.g., Aracri et al., 2017). For EPSPs, we used a 2 mV threshold to select events caused by synchronous activation of at least 2-3 pyramidal neurons. Such estimate is based on the following argument. The average unitary EPSP amplitude measured on cell soma is ~0.5 mV in mammalian PFC slices (Povysheva et al., 2006), therefore the minimum number of events possibly causing a 2 mV EPSP ($EPSP_{2mV}$) is 4. To be caused by a single neuron, an $EPSP_{2mV}$ should be underlain by simultaneous activation of 4 synaptic boutons. We estimate this event to have a probability lower than 0.001. In fact, the probability of two pyramidal neurons forming reciprocal synapses steeply decreases with distance, and multiple synapses are only observed between close neurons (~50 μm). Within this distance, a given pyramidal neuron receives 4 or more contacts by ~7% of the surrounding neurons (Braitenberg and Schütz, 1998). By assuming each pyramidal neuron has the same probability of firing an action potential, at any given time approximately 7% of the firing events potentially leading to glutamate release onto a given neuron will involve a neuron forming multiple synaptic contacts with the neuron under recording. Each AP elicits glutamate release from each synaptic bouton in approximately 30% of the cases, as the probability of transmission of ~0.3 among neocortex pyramidal cells (Koch, 2000). Thus, the probability of a single AP to stimulate release simultaneously from 4 sites is in the order of $(0.3)^4=0.0081$. Hence, the fraction of $EPSP_{2mV}$ generated by a single presynaptic neuron should be in the order of 0.07×0.0081, i.e., less than 1/1000, and much lower for larger EPSPs.

2.12. Post-recording morphological characterization

Neurobiotin (1 mg/ml) was added to the pipette solution in a fraction of patch-clamp experiments. Slices were fixed post-recording in PB with 4% paraformaldehyde (24-48 h, at 4 °C). Next, they were washed with PBS and incubated with 0.05 M NH_4Cl for 30 min, to block the residual aldehyde groups from fixation. After treatment with 2% bovine serum albumin (BSA) and 0.05% Triton X-100 in PBS (2 h, RT), sections were incubated with Alexa-488-labeled streptavidin (1:200; Molecular Probes, Eugene, OR) in the same solution (3 h, RT). After washing with PBS, slices were transiently mounted on slides with PBS/glycerol. After verifying the success of cell labeling, they were incubated at 4°C overnight with anti-PV (1:2000) and anti-SOM (1:100-200), in PBS with 2% BSA and 0.05% Triton X-100. After rinsing, slices were incubated with the secondary antibodies (3 h, RT): $CF^{TM}568$-conjugated donkey anti-mouse (Sigma) and Cy5-conjugated donkey anti-rabbit (Jackson ImmunoResearch), both at 1:200 in PBS with 2% BSA. Finally, sections were washed with PBS and mounted on gelatin-coated slides with Vectashield supplemented with DAPI (VectorLabs, Burlingame, CA) for analysis with a Nikon Ti-E/A1+ high performance inverted confocal laser scanning microscope (Nikon, Tokyo, Japan). 3D neuron reconstruction was performed using the Simple Neurite Tracer plugin in Fiji ImageJ on the green channel Z-stack, holding the signal for Alexa-488-labeled streptavidin.

2.13. Statistical analysis

Unless otherwise indicated, data are given as mean values ± SEM. Comparisons between two populations of data were conducted with paired or unpaired Student's t-test, as indicated, after verifying normality (Shapiro-Wilk test) and variance homogeneity (F test). In case of unequal variances, the Welch's correction was applied. The Mann-Whitney test was used to compare medians in case of non-normal distributions. Multiple comparisons were analyzed with one-way ANOVA (with post-hoc Bonferroni's test), after verifying normality

(Shapiro-Wilk test) and variance homogeneity (Brown-Forsythe test). For synaptic events recorded in individual cells, the non-normal distributions of events' amplitudes and inter-event intervals under different treatments were compared with the Kolmogorov-Smirnov (KS) test for two samples. The level of statistical significance in the figures is indicated as follows: NS: not significant; $0.05 \geq p^* > 0.01$; $0.01 \geq p^{**} > 0.001$; $p^{***} \leq 0.001$.

3. RESULTS

3.1. Effects of $\beta2^{V287L}$ on neocortex thickness and neuronal populations

Neocortex thinning in frontal regions has been observed in children with frontal lobe epilepsy (Lawson et al., 2002; Widjaja et al., 2011; Rahatli et al., 2020), but not investigated in depth in murine models of ADSHE. Hence, we first analyzed cortical thickness and neuronal populations in mice from P9 to P120. In SS, thickness was similar in different genotypes, whereas in PFC $\beta2^{V287L}$ presented a ~10% thickness decrease as early as P12 (**Supplementary Fig. 1A-B**). We next quantified the neuronal populations in layer V at P60, by stereological cell counts on sections stained with thionin (**Supplementary Fig. 1C**), to estimate the total neuronal population on the whole section volume. In both SS (not shown) and PFC (**Supplementary Fig. 1D-D'**), no significant differences were observed between genotypes.

Because the total cell count could mask changes in the comparatively small GABAergic population, we analyzed total GABAergic expression by GAD67 immunofluorescence (Esclapez and Houser, 1999). Representative images from Control and $\beta2^{V287L}$ mice are respectively shown in **Fig. 1A and 1A'**. Densitometric analysis was carried out in layers II/III and V, in slices from Control and $\beta2^{V287L}$ mice (P60). The signal intensity was normalized to the total cell count. No significant differences were found between genotypes in either supra- or infragranular layers of PFC (**Fig. 1B**) and SS (not shown). Next, we compared the main GABAergic populations in layer V, i.e. PV+ and SOM+ neurons. We focused on layer V because these cell populations are abundant in this layer, in which both have a recognized role in control and spread of excitability (Trevelyan et al., 2006; Cammarota et al., 2013; Parrish et al., 2019). In contrast, the density of SOM+ cells is much lower in layers II/III. In addition, these results provide a morphological comparison with our patch-clamp experiments in layer V (see 3.3 and later sections). PV+ neurons were counted by stereology on sections labeled with immunoperoxidase method and counterstained with thionin, to better recognize layer V.

Typical images at different magnification are shown in **Fig. 1C, D**. The corresponding average stereological cell counts are reported in **Fig. 1E** for the entire PFC and for PFC layer V. No significant differences were observed between mice expressing or not $\beta2^{V287L}$. Similar results were obtained in SS (not shown).

Because poor SOM+ cell labeling was obtained with the immunoperoxidase method, we next compared PV+ and SOM+ cell populations by immunofluorescence. Representative images of PFC layer V sections labeled for PV are shown in **Fig. 1F** (Control) and **1F'** ($\beta2^{V287L}$), while the average cell counts are reported in **Fig. 1G**, for total PFC and PFC layer V. In agreement with stereological cell counts, no significant differences were observed between genotypes in PV+ cell counts. Similar results were obtained with SOM+ cells. Representative immunofluorescent PFC layer V images are shown in **Fig. 1H** (Control) and **1H'** ($\beta2^{V287L}$), while the average cell counts in PFC and PFC layer V are displayed in **Fig. 1I**. In brief, expression of $\beta2^{V287L}$ did not alter the numerousness and balance of PV+ and SOM+ neurons in PFC. We conclude that $\beta2^{V287L}$ does not cause major alterations in neocortex structure and neuronal populations, except for an overall decrease in PFC thickness. We attribute the latter to a smaller neuropil volume, as it was not accompanied by a significant decrease of neuronal counts.

3.2. $\beta2^{V287L}$ did not alter cholinergic innervation in PFC

We next studied whether the transgene specifically affected the cholinergic system, which could alter ACh release in wakefulness and sleep. At P90, ChAT+ neurons were estimated by stereological cell counts in LDT, PPT (**Fig. 2A** and **2A'**, respectively for Control and $\beta2^{V287L}$) and NBM (**Fig. 2B** and **2B'**, respectively for Control and $\beta2^{V287L}$). In these nuclei, the average number of cholinergic cells was not significantly different between genotypes (**Fig. 2C**). Analogous results were obtained at P60 (not shown). The cholinergic innervation in the neocortex was first investigated by ChAT immunoperoxidase labeling at P90 (**Fig. 2D, E**).

Once again, no differences were observed between genotypes in PFC layers II/III and V (**Fig. 2F**) and SS (not shown). Next, we carried out a densitometric analysis of VAChT immunofluorescent labeling, which allows better detection of the rare cholinergic synaptic puncta (Aracri et al., 2010 and references therein). Typical images from Control and $\beta2^{V287L}$ are respectively displayed in **Fig. 2G** and **2G'**. In agreement with the results obtained with immunoperoxidase-stained sections, VAChT quantification revealed no difference in cholinergic innervation between Control and $\beta2^{V287L}$ both in the entire PFC and in PFC layer V (**Fig. 2H**). This method was also used to study the relationship of VAChT+ varicose fibers and puncta with PV+ or SOM+ neurons in PFC layer V of Control mice to identify a possible disparity in the normal cortical circuit. **Fig. 2I** and **2J** show representative images of double-immunolabeling of VAChT combined respectively with PV and SOM. The quantitative distribution of VAChT onto the cell bodies of PV+ and SOM+ neurons was evaluated by applying 3D analysis on confocal microscope z-stacks with ArivisVision4D software (see also **Fig. 3A**). Normalizing the number of terminals by the number of cells of either type showed no significant difference between the number of cholinergic contacts on PV+ neurons and SOM+ cells (**Fig. 2K**), suggesting no specific association of cholinergic fibers with the main layer V GABAergic populations. Considering the diffuse nature of cholinergic innervation, in which axonal varicosities accompany pyramidal cell dendrites and GABAergic cell bodies, but often do not form synaptic contacts (especially on GABAergic cells; Henny and Jones, 2008; Aracri et al., 2010), we consider that large differences between genotypes are unlikely and thus do not present a detailed analysis for $\beta2^{V287L}$.

3.3. The main neuronal types in Fr2 layer V

From an electrophysiological standpoint, three populations of neurons largely prevail in Fr2 layer V: regular spiking pyramidal neurons, FS interneurons and regular spiking non-pyramidal (RSNP) cells. Pyramidal neurons display classic firing properties, with no difference

between Control and β2^{V287L} (Amadeo et al., 2018), and will not be further characterized here. FS neurons are essentially PV+ cells (Aracri et al., 2017) and presented no significant electrophysiological difference between genotypes (**Table 2**). RSNP neurons have V$_{rest}$ around -70 mV; AP frequency of ~50 Hz (200 pA stimulus), with more pronounced adaptation compared to FS cells; spike width of ~1.8 s (at half-maximal amplitude) and shallow after-hyperpolarization (**Table 2**). In analogy with other neocortex regions (Tremblay et al., 2016), a similar number of PV+ and SOM+ cells were observed in Fr2 layer V (**Fig. 1F-I** and **Fig. 3A**), which led us to hypothesize that the common RSNP cells largely belong to the SOM+ population. In fact, post-recording morphological characterization revealed a bitufted or multipolar shape accompanied by SOM immunoreactivity (**Fig. 3B-C**). Typical RSNP cell firing and the average stimulus-frequency relationship for a representative group of age-matched Control and β2^{V287L} neurons are shown in **Fig. 3D-E,** revealing no statistical difference between genotypes in firing features (see also **Table 2**). Finally, RSNP cells displayed no response to 100 μM 5-HT focally applied onto the cell soma (**Fig. 3F**). In conclusion, we classify RSNP cells as a SOM+ GABAergic population not expressing the ionotropic serotonin receptor 5HT3a (5HT3aR), and thus likely belonging to the Martinotti class (Nigro et al., 2018).

3.4. β2^{V287L} decreased the glutamatergic input to FS neurons

We next studied whether the transgene produced permanent changes in the prefrontal synaptic network, by examining the spontaneous EPSC and IPSC events in pyramidal, FS and RSNP neurons. EPSCs were recorded as inward currents at -70 mV (i.e. close to E$_{GABA}$; **Fig. 4A**), while IPSCs from pyramidal neurons were recorded as outward currents at +10 mV, (i.e. close to E$_{rev}$ for ionotropic glutamate receptors; **Fig. 4B**), by using a high-Cs$^+$ pipette solution. IPSCs in GABAergic neurons were recorded at -70 mV, with a high-Cl$^-$internal solution, in the presence of AP5 and CNQX (see *2.10*). To warrant the best compromise between maturity of prefrontal circuits and feasibility of patch-clamp recording in brain slices, experiments were

generally carried out after the 4th postnatal week, when the synaptic networks had reached a steady state. This is illustrated in **Fig. 4C**, showing the average EPSC frequency in pyramidal, FS and RSNP cells, at different postnatal times. In both Control and $\beta 2^{V287L}$ mice, no significant change in the spontaneous synaptic activity was observed during the 2nd postnatal month. Nonetheless, because in RSNP neurons a trend to EPSC frequency decrease was observed after the 4th week (although not statistically significant), we further characterized the long-term trend by carrying out several experiments during the 4th month (>P90; **Fig. 4C**). This made us confident that, also in RSNP cells, the basal excitatory input is essentially stable after the first postnatal month, irrespective of genotype.

On average, the basal EPSC frequency was approximately halved in FS cells from $\beta 2^{V287L}$ mice. Representative EPSCs recorded on FS neurons are shown in **Fig. 4D**. The overall results on spontaneous synaptic events recorded between the 5th postnatal week and P60 are summarized in **Fig. 4E.** The decrease of EPSC frequency was not accompanied by a significant alteration of EPSC amplitudes, as the average of the median amplitudes was 10.0 ± 0.61 pA in Control (tTA; n = 22 neurons) and 11.2 ± 0.63 pA in $\beta 2^{V287L}$ (n = 31; NS with unpaired t-test). The effect was abolished when $\beta 2^{V287L}$ expression was silenced by administering doxycycline up to P15 (**Fig. 4E**, hatched bars), which covers the most active phase of postnatal synaptogenesis. In agreement with the observed decrease of excitatory drive in FS cells from $\beta 2^{V287L}$ mice, the spontaneous IPSC frequency was significantly lower in pyramidal cells carrying the transgene (**Fig. 4E**), which further points to partial disinhibition of layer V circuit. No difference was found between genotypes in the EPSC frequencies of pyramidal and RSNP neurons (**Fig. 4E**), nor in the IPSC frequency (**Fig. 4E**) or amplitude (not shown) of FS and RSNP cells. Detailed statistics are reported in the figure legend.

In conclusion, expressing $\beta 2^{V287L}$ throughout brain development leads to a long-term decrease of the excitatory input to FS cells in prefrontal layer V. This could facilitate seizures by weakening the recurrent inhibition that normally restrains pyramidal cells' excitability.

3.5. β2[V287L] decreased the miniature EPSCs (mEPSCs) frequency in FS neurons.

In PFC, we previously found the spontaneous EPSCs on pyramidal and FS cells are essentially glutamatergic events (Aracri et al., 2013; 2015), in agreement with neuroanatomical results. In fact, the main alternative excitatory input that could produce inward EPSCs at -70 mV is the cholinergic. However, only ~4% of synaptic boutons in layer V of rodents' associative cortices are cholinergic, and even less form *bona fide* synapses (Turrini et al., 2001). Most of these synapses are formed on pyramidal neurons, whereas cholinergic synapses on PV+ cells are sporadic (Henny and Jones, 2008; Aracri et al., 2010). Nonetheless, the lower EPSC frequency observed in FS cells carrying β2[V287L] is unlikely to be caused by a major overall decrease of pyramidal cell activity, as the spontaneous EPSC frequency in pyramidal cells was not different between genotypes (**Fig. 4E**). To better distinguish the possible effects of the network spiking activity from those produced by specific alterations of the physiology of excitatory synapses on FS cells, we studied mEPSCs. These were revealed by blocking cell firing with 1 μM TTX, as shown in **Fig. 5A** (Control) and **Fig. 5B** (β2[V287L]). The respective distributions of interevent intervals and current amplitudes are reported in **Fig. 5C** and **5D**. On average, the mEPSC frequency in β2[V287L] mice was approximately halved compared to Control (**Fig. 5E**), with no concomitant decrease of the median mEPSC amplitudes (**Fig. 5F**). These results suggest that β2[V287L] lowers the rate of spontaneous glutamate release onto FS cells, without altering the quantal amplitude.

3.6. Distribution of excitatory and inhibitory synapses in mice expressing or not β2[V287L].

The observed decrease of EPSC frequency in FS neurons of β2[V287L] mice could reflect a lower density of excitatory terminals in these cells, or a lower individual probability of release, or both. To better discriminate between these possibilities, we studied the distribution of synaptic terminals in neocortical layer V. First, glutamatergic terminals were analyzed by

immunoperoxidase labeling of VGLUT1 (**Supplementary Fig. 2A**). VGLUT1 essentially labels intracortical glutamatergic fibers (discussed in Kameda et al., 2012) and is by far the main vesicular glutamate transporter in neocortex, including Fr2 (Aracri et al., 2013). In both PFC (**Supplementary Fig. 2**) and SS (not shown), no differences were observed between Control and $\beta2^{V287L}$ in total VGLUT1 expression in layers II/III and V, as assessed by optical density. Representative images for layer V are shown in **Supplementary Fig. 2A (Control**) and **Supplementary Fig. 2A' (**$\beta2^{V287L}$). Moreover, Golgi-Cox analysis revealed no statistical difference between genotypes in spine density and dendritic complexity in pyramidal neurons of PFC layers II/III and layer V (**Supplementary Fig. 3**). Therefore, the overall architecture of glutamatergic transmission was not altered by $\beta2^{V287L}$, in agreement with the results obtained with spontaneous EPSCs on pyramidal neurons.

Next, we investigated the association of VGLUT1 terminals with PV+ (**Fig. 6A-D**) and SOM+ (**Fig. 6E-H**) cell bodies, by applying 3D analysis on confocal microscope images acquired from immunofluorescent sections. In cortical interneurons, a significant fraction of excitatory synapses is found on proximal dendrites and somata (Ichikawa et al., 1985; Kameda et al., 2012; Hioki, 2015). For the sake of brevity, only the results obtained in PFC layer V are displayed. Representative images of VGLUT1/PV double immunolabeling are shown in **Fig. 6A.** On average, the number of VGLUT1+ terminals contacting PV+ cell bodies was higher in $\beta2^{V287L}$ mice (**Fig. 6B-D**). In contrast, the number of VGLUT1 terminals on SOM+ cells was very similar in mice carrying or not $\beta2^{V287L}$ (**Fig. 6E-H**). These results show that the lower EPSC frequency observed in $\beta2^{V287L}$ FS cells was not accompanied by a major decrease of excitatory innervation. On the contrary, they suggest some compensatory effect is operant, in mutant mice. However, discriminating whether the glutamatergic synapses on $\beta2^{V287L}$ PV cells have a lower efficacy of release, or the formation of synaptic contacts during synaptogenesis is disfavored, or both, will require precise determinations of pre- and postsynaptic structures (see Discussion).

An analogous procedure was applied to study the GABAergic terminals, which were identified by labeling the vesicular GABA transporter VGAT. Representative images are shown for VGAT/PV (**Fig. 7A**) and VGAT/SOM (**Fig. 7E**) immunolabeling, in PFC layer V. In brief, no difference between genotypes was observed in the number and distribution of VGAT+ terminals on the cell bodies of PV+ (**Fig. 7B-D)** and SOM+ (**Fig. 7F-H)** neurons. In addition, densitometric analysis was applied to the widely distributed α1 GABA$_A$ subunit. In both PFC (**Supplementary Fig. 4)** and SS (not shown), α1 expression was considerably higher in supragranular layers, with no significant differences between Control and β2^{V287L} (**Supplementary Fig. 4A-A', and 4B).** These results rule out major alterations of the neocortical GABAergic system in mice carrying the transgene.

3.7. Effect of nAChR activation on EPSCs and IPSCs in pyramidal and FS neurons

The lower glutamatergic drive observed in FS neurons of β2^{V287L} mice points to long-term alteration of prefrontal excitability. Because ADSHE seizures tend to occur during NREM sleep, we asked how these abnormal networks respond to nAChR stimulation, as a high cholinergic tone is a hallmark of the waking state, as compared to NREM sleep (Jones, 2020). As in other neocortex regions, in Fr2 heteromeric nAChRs are widely expressed at presynaptic as well as somatic sites of different neuronal populations (Aracri et al., 2010, 2013, 2017). Hence, we first tested by immunofluorescence whether β2^{V287L} modified the overall β2* nAChR expression in PFC and its distribution in synaptic boutons. The latter was analyzed by studying β2 colocalization with synaptophysin, widely expressed in synaptic vesicle membranes (Rehm et al., 1986). The results obtained in PFC at P60 are shown in **Supplementary Fig. 4C-G**. No significant difference was observed between genotypes in overall β2* nAChR expression (in agreement with previous tests with labeled epibatidine; Manfredi et al., 2009), nor in its distribution in synaptic terminals.

Next, the functional effect of nAChR activation on layer V was tested with nicotine, for two reasons. First, using ACh requires adding muscarinic antagonists, whose effects on nAChR subtypes are ill-defined (e.g., Zwart and Vijverberg, 1997). Second, nicotine has been used to control the symptoms in ADSHE patients (Becchetti et al., 2020). Nicotine was applied in the bath at 10 µM, which corresponds to the peak of nAChR 'window current', thus producing maximal steady state activation of heteromeric nAChRs (Fenster et al., 1997). Bath perfusion allowed to stimulate at the same time the entire synaptic complement and the cell soma of the tested neuron.

Somatic nicotinic currents were identified as inward desensitizing whole-cell currents, at -70 mV. In murine PFC, somatic nicotinic currents are rare in pyramidal cells (e.g., Couey et al., 2007), whereas in FS neurons they tend to subside after the first postnatal month, at least in Fr2 (Aracri et al., 2017). In the present experiments, they were observed in ~20% of pyramidal neurons (with average current amplitudes in the order of 30 pA) and less than 10% of FS cells (average current amplitudes ~15 pA), with scarce difference between genotypes.

On the other hand, the sensitivity of synaptic events to nAChR stimulation is maintained in mature prefrontal networks. In pyramidal neurons, a substantial increase of EPSC frequency was observed in both genotypes, in agreement with the wide distribution of $\alpha 4\beta 2$ nAChRs in glutamatergic terminals in Fr2 layer V (Aracri et al., 2013). Representative experiments are shown in **Fig. 8A** (Control) and **Fig. 8B** ($\beta 2^{V287L}$), with the corresponding distributions of interevent intervals being overlayed in **Fig. 8C**. The average overall effects are shown in **Fig. 8D** (left part). Nicotine also stimulated IPSC frequency, in pyramidal cells, and the average effects in Control and $\beta 2^{V287L}$ are shown in **Fig. 8D** (right part). Noteworthy, the median increase was 28% in Control and 67% in $\beta 2^{V287L}$ (**Fig. 8I**), suggesting that the nAChR stimulation of IPSCs was comparatively stronger in $\beta 2^{V287L}$ mice.

The above reasoning was substantiated by testing the excitatory input to FS neurons. Representative EPSC recordings in FS cells are shown in **Fig. 8E** (Control) and **Fig. 8F**

($\beta2^{V287L}$), with the corresponding distributions of interevent intervals being overlayed in **Fig. 8G**. The average overall effects are shown in **Fig. 8H.** Nicotine (10 μM) increased the EPSC frequency in both genotypes, and the effect was significantly stronger in $\beta2^{V287L}$ (+15% in Control and +39% in $\beta2^{V287L}$; **Fig. 8I**). No significant effects were observed on EPSC amplitudes (**Fig. 8J-K**).

In conclusion, nicotine produced a larger inhibitory input to pyramidal cells in $\beta2^{V287L}$. We attribute part of this effect to the stronger stimulus of glutamatergic release onto FS neurons carrying the transgene (**Fig. 8I**). The possible contribution of other mechanisms is discussed later. Overall, nAChR stimulation partially rescues the defective excitatory drive onto FS neurons expressing $\beta2^{V287L}$, thus bringing layer V synaptic balance closer to the Control level.

3.8. Effect of nAChR activation on RSNP cells

Differently from pyramidal and FS neurons, in >90% of RSNP neurons nicotine elicited somatic inward currents with slow desensitization. Typical recordings at −70 mV are displayed in **Fig. 9A** (Control) and **9B** ($\beta2^{V287L}$). The respective average peak whole-cell currents are plotted in **Fig. 9C** (left panel). To rule out the variability caused by different cell sizes, **Fig. 9C** (right panel) also reports the corresponding average current densities (i.e. the peak whole-cell currents divided by the cell capacitances). The peak current density in the presence of nicotine was approximately doubled in mice carrying the transgene, which is consistent with the 'gain of function' properties conferred by $\beta2^{V287L}$ on α4β2 nAChRs expressed in heterologous systems. To better define the heteromeric nAChR subtype expressed by RSNP cells, we tested the effect of 1 μM DHβE, which is known to block α4* nAChRs. Differently from pyramidal and FS cells (Aracri et al., 2010; 2013), in RSNP cells 1 μM DHβE did not cause full block of the nicotinic current (**Fig. 9D**), which was only obtained with 30 μM DHβE (**Fig. 9E**). The average nicotinic peak current densities measured with either 1 or 30 μM DHβE are shown in **Fig. 9F**. The poor sensitivity to DHβE of the nAChRs expressed in RSNP cells can be

interpreted in the light of recent results obtained in mouse neocortex, showing that layer V Martinotti cells mainly express heteromeric α2* nAChRs (Hilscher et al., 2017). These are known to be blocked by DHβE concentrations >10 μM, when tested with 10 μM nicotine (Chavez-Noriega et al., 1997). We conclude that RSNP neurons express somatic non-α4* nAChRs up to the adult age, and the ensuing whole-cell nicotinic currents are larger in mice carrying $\beta2^{V287L}$. This effect could increase the inhibition produced by these cells on pyramidal neurons when the cholinergic tone is high.

3.9. $\beta2^{V287L}$ effects on layer V excitability

The experiments illustrated in Fig. 3 suggest that layer V circuit is partially disinhibited in mice expressing $\beta2^{V287L}$, because of a lower glutamatergic input to FS interneurons. Following this lead, we used layer V pyramidal cells as a probe to verify whether transgene expression was accompanied by network hyperexcitability and whether the effect was sensitive to nicotine. Excitatory postsynaptic potentials (EPSPs) and AP firing were first recorded in neurons maintained around -70 mV, in ACSF. Next, moderate circuit disinhibition was induced by adding 2 μM bicuculline. This concentration is close to the IC_{50} for $GABA_A$ receptors (Ueno et al., 1997) and higher concentrations are usually necessary to elicit burst activity without further stimulation (e.g., Gutnick et al., 1982; Wong and Traub, 1983). Finally, 10 μM nicotine was added in the presence of bicuculline. In Control neurons, spontaneous APs were rare in ACSF, and only 1 neuron out of 17 showed sustained firing activity. In the others, 2 APs were observed during 32 min overall recording. On bicuculline addition (5 min), both WT (**Fig. 10A**) and tTA (**Fig. 10C**) displayed a modest increase in the frequency of the spontaneous EPSPs, with the sporadic appearance of larger depolarizing events that rarely led to spike bursts (5 out of 17 neurons displayed firing activity, during ~90 min overall recording in the presence of bicuculline). Application of 10 μM nicotine considerably increased the frequency of large depolarizing events, which generally (78% of the cells) took a regular oscillatory pattern around

0.5 Hz (**Fig. 10A-C**), which in ~50% of the cells led to spiking activity (an example is shown in **Fig. 10A-B**). We attribute this effect to the powerful stimulation exerted by nAChR activation on glutamatergic transmission between pyramidal neurons (**Fig. 8**). In fact, recurrent excitatory connections between pyramidal neurons are known to sustain the 'up' phase of the spontaneous 0.5 Hz rhythm in layer V of neocortex slices (Sanchez-Vives and McCormick, 2000).

In $\beta2^{V287L}$ also, spontaneous firing was rare in ACSF (1 cell out of 14). However, a higher EPSP activity was observed with respect to Control, which in 20% of neurons took a ~0.5 Hz oscillatory rhythm (**Fig. 10D**). More specifically, the average frequency of EPSP events with amplitudes $\geq$ 2 mV (EPSP$_{2mV}$) is shown in **Fig. 10E** for tTA and $\beta2^{V287L}$ slices bathed with ACSF. A 2 mV threshold was chosen to select EPSP events reflecting the synchronous activation of at least 2-3 pyramidal neurons (as explained in *2.11*), thus providing a minimum cue of network synchronization. The frequency of EPSP$_{2mV}$ events was more than doubled in $\beta2^{V287L}$, compared to Control. These results indicate a higher degree of network synchronization in slices carrying the transgene, in basal conditions. Application of nicotine in the presence of bicuculline increased the frequency of EPSP$_{2mV}$ also in $\beta2^{V287L}$, but spiking activity was absent (**Fig. 10F**). Stimulation of firing was obtained in $\beta2^{V287L}$ only by applying nicotine in presence of 10 μM bicuculline (**Fig. 10F**).

We attribute the smaller effect of nicotine on disinhibited $\beta2^{V287L}$ slices to the combined effects on FS and RSNP cells, as both cell types contribute to feedforward inhibition during epileptiform activity in brain slices (Parrish et al., 2019). The comparatively stronger effect of nicotine on the glutamatergic input to FS cells carrying $\beta2^{V287L}$ (**Fig. 8**) partially rescues the synaptic deficit. Moreover, overstimulation of somatic currents in RSNP cells carrying the transgene may produce more effective dendritic inhibition in pyramidal cells.

4. DISCUSSION

We analysed prefrontal synaptic transmission and excitability in brain slices from a murine model of ADSHE that displays major features of the human pathology, namely epileptic seizures during NREM sleep. Expression of $\beta2^{V287L}$ throughout development led to a defective glutamatergic input to layer V FS cells, which was accompanied by a higher sensitivity of regular spiking SOM+ cells to nAChR activation. These functional alterations were associated to hyperexcitability in prefrontal layer V. In analogy with other ADSHE models (Klaassen et al., 2006; Zhu et al., 2008; O'Neill et al., 2013), no major change in brain structure was observed in $\beta2^{V287L}$ mice. Nonetheless, these animals displayed a ~10% decrease of PFC thickness, which resembles the frontal cortex thinning observed in young patients (Lawson et al., 2002; Widjaja et al., 2011; Rahatli et al., 2020). Stimulation of nAChRs with nicotine produced a partial functional rescue of the synaptic deficit and dampened hyperexcitability in vitro.

4.1. The effect of $\beta2^{V287L}$ on layer V synaptic network

The main synaptic effect of constitutive $\beta2^{V287L}$ expression was a long-term decrease of spontaneous and miniature EPSC frequency in layer V FS cells, with no concomitant alteration of mEPSC amplitude. This is usually considered evidence of a lower average probability of transmitter release (van der Kloot and Molgó, 1994), which could depend on a decreased number of release sites, or a lower unitary probability of release, or a combination of these factors. Because the total VGLUT1 expression did not change in $\beta2^{V287L}$ mice and the number of VGLUT1 terminals adjacent to PV+ cells increased, we attribute the transgene effect to a defective glutamate transmission between pyramidal and FS neurons. At the present stage, we cannot say whether the effect entirely depends on decreased probability of release per synaptic bouton, or to impaired formation of well differentiated synaptic structures, or both. Clarifying this issue will need a precise quantification of the *bona fide* glutamatergic synapses onto PV+

cells. This may require electron microscopy image reconstruction, as is increasingly clear that a simple proximity criterion for pre- and postsynaptic structures observed by immunofluorescence is not fully adequate (Kasthuri et al., 2015).

From a physiological standpoint, prefrontal slices expressing $\beta2^{V287L}$ were more likely to display network synchronization, when disinhibited by submaximal bicuculline concentrations (**Fig. 9**), in agreement with the fact that FS PV+ neurons potently regulate surround inhibition of pyramidal neurons (e.g., Trevelyan et al., 2006; Cammarota et al., 2013). Moreover, the fact that defective activation of FS cells facilitates network synchronization is consistent with *in vivo* results showing that activating PV+ cells decreases slow-wave activity in murine neocortex (Funk et al., 2017). Therefore, in some forms of ADSHE, the propensity for developing neocortical seizures may depend on a permanent impairment of the glutamatergic drive onto FS neurons.

Stimulation of nAChRs by nicotine produced a higher increase of inhibitory tone in $\beta2^{V287L}$, as compared to Control (**Fig. 8**). We attribute this effect to the partial rescue produced by nicotine on the excitatory deficit in FS cells, possibly accompanied by the higher sensitivity of RSNP cells in $\beta2^{V287L}$. Interestingly, previous studies in knock-in $\beta2^{V287L}$ mice showed a larger nicotine-induced GABA release from synaptosomes compared to the controls (O'Neill et al., 2013). This suggests that an intrinsic presynaptic component may be also present in the effect of $\beta2^{V287L}$ on GABA release. However, the lack of information about spontaneous release in the absence of stimulation and the interaction of different neuronal populations in the knock-in model prevents to bring the comparison too far. We notice nonetheless that in knock-in $\beta2^{V287L}$ mice the phenotypic alterations are mild (Xu et al., 2011), compared to both transgenic rats (Shiba et al., 2015) and mice (Manfredi et al., 2009). Because in transgenic animals no major change was observed in membrane expression of $\beta2*$ and $\alpha7*$ nAChRs, nor in the relative subunit composition (Manfredi et al. 2009; Shiba et al., 2015; **Supplementary Fig. 4**), we believe a direct effect of the different gene dosage on the synaptic circuit is unlikely. Whether

the difference between knock-in and transgenic animals depends on strain/species, or on stronger effects produced by the transgene on the β2* nAChR-dependent regulation of transcriptional program in the neocortex (Jung et al., 2016) remains to be determined.

4.2 Possible action of β2^{V287L} during synaptogenesis

We can advance two working hypotheses to explain why β2^{V287L} selectively decreases the glutamatergic input on FS cells. The first turns on the fact that nAChRs modulate neurotransmitter release because of their permeability to Ca^{2+} (which can activate calcium release from intracellular stores) and because they promote activation of voltage-gated Ca^{2+} channels by depolarization (Sharma and Vijayaraghavan, 2003; Dickinson et al., 2008). Hence, hyperactive mutant nAChRs could cause abnormal elevation of presynaptic calcium, which often leads to long-term synaptic depression, as was demonstrated in the calix of Held (Billups and Forsythe, 2002), motor nerve terminals (David and Barrett, 2003) and mouse neocortex neurons (Sambri et al., 2020). The effect would be maximal in the powerful excitatory-to-inhibitory connections (e.g., Molnár et al., 2008). The above argument suggests that the increased density of glutamatergic boutons we observed around the PV+ neuron somata in β2^{V287L} mice is a compensatory response which sustains recurrent inhibition in layer V.

Second, β2^{V287L} expression could alter the balance between excitatory synapses targeting pyramidal and basket cells, by acting during PFC maturation. Available evidence about the role of nAChRs in neocortex synaptogenesis mostly regards glutamatergic synapses between pyramidal neurons. In rodents, β2 and α7 nAChR subunits peak around P14, when they cooperate in regulating dendritic spine maturation through Ca^{2+} signals affecting the actin cytoskeleton (Ballestreros-Yanez et al., 2010; Lozada et al., 2012; Lin et al., 2014; Molas and Dierssen, 2014; Kang et al., 2015). In fact, we have evidence that heteromeric nAChRs regulate glutamate release on pyramidal neurons since the first postnatal week (Brusco and Becchetti, unpublished results). Unfortunately, much less is known about whether and how nAChRs

regulate the formation of excitatory synapses on PV+ GABAergic neurons. The latter process is specifically controlled by the postsynaptic tyrosine kinase receptor ErbB4 and its presynaptic secreted ligands, especially neuregulin 1 (NRG1; Krivosheya et al., 2008; Fazzari et al., 2010; Ting et al., 2011) and 3 (NRG3; Müller et al., 2018). In rodents' neocortex, ErbB4 is almost exclusively expressed by GABAergic neurons (Bean et al., 2014) since early embryonic stages (Yau et al., 2003), and deleting ErbB4 or NRG impairs the formation and efficacy of excitatory synapses on PV+ cells (Fazzari et al., 2010; Ting et al., 2011; Müller et al., 2018). Recently, nAChRs have been found to regulate ErbR4-dependent signaling in the neocortex. Both homo- and heteromeric nAChRs contribute to stimulate ErbB4 in GABAergic neurons, probably by presynaptic activation of its ligand NRG3, which is proteolytically activated by nAChR-dependent calcium signals (Zhou et al. 2018). Based on these premises, we hypothesize that hyperactive $\beta2^{V287L}$-containing nAChRs could overstimulate the NRG/ErbB4 pathway during synapse formation, thus altering the balance and functionality of glutamatergic synapses on FS PV+ cells. Unbalance of the glutamatergic network could be facilitated by the $\beta2^{V287L}$-dependent delay of the postnatal GABAergic 'shift' (Amadeo et al. 2018). This may prolong the early depolarizing effect of GABA during synaptogenesis, which stimulates the activity-dependent maturation of the excitatory network by favoring current flow through NMDA receptors (Wang and Kriegstein, 2008; Anastasiades and Butt, 2012).

4.3. Effect of nAChR stimulation and relation of ADSHE seizures with NREM sleep.

A full explanation of the ADSHE phenotype requires understanding why seizures tend to occur during NREM sleep. Our results demonstrate that a synaptic unbalance is present in $\beta2^{V287L}$ mice in basal conditions, i.e. in the absence of neuromodulation. Activation of the ascending cholinergic system is a major feature of wakefulness and REM sleep, as compared to NREM sleep (Jones, 2020). Our results suggest that no major alteration is caused by $\beta2^{V287L}$ on the cholinergic innervation in PFC. Assessing subtle differences in the association of

cholinergic presynaptic structures with specific neuronal populations will require electron microscopy studies on serial sections. Nonetheless, we observed a clear functional difference between genotypes in prefrontal excitability under nAChR stimulation. Expression of $\beta 2^{V287L}$ was correlated with a higher degree of local synchronization of excitatory activity in basal conditions as well as in the presence of moderate circuit disinhibition with bicuculline, in line with the lower efficacy of the inhibition produced by FS cells. In contrast, nicotinic stimulation boosted excitability in Control slices, but not in $\beta 2^{V287L}$. We attribute the dampening exerted by nicotine on $\beta 2^{V287L}$ network excitability to the simultaneous effects produced by the drugs on both FS and RSNP neurons, as recent work has demonstrated that PV+ and SOM+ GABAergic neurons cooperate in controlling feedforward inhibition at the front of epileptiform waves in vitro (Parrish et al., 2019). First, nAChR activation decreased the synaptic unbalance observed in $\beta 2^{V287L}$ mice, as in these nicotine was more effective in stimulating excitatory input to FS cells, as compared to Control (**Fig. 8I**). Second, differently from FS cells, the majority of SOM+ RSNP cells displayed somatic nicotinic currents, whose amplitude was larger in cells carrying $\beta 2^{V287L}$ (**Fig. 9**). Hence, nAChR activation could potentiate the inhibition produced by these cells on pyramidal cell dendrites. A full understanding of the ADSHE relation to sleep will also require investigating the role of thalamic GABAergic neurons, a currently neglected aspect. Recent microdialysis studies in rats expressing $\alpha 4^{S286L}$ (corresponding to the human $\alpha 4^{S284L}$) suggest that impaired intrathalamic GABAergic inhibition can lead to increased glutamatergic release from thalamocortical fibers in M2 premotor cortex, which could contribute to cortex hyperexcitability (Fukuyama et al., 2020). Whether these mechanisms are also operant in other ADSHE models is unknown.

4.4. Conclusions

Our results could help to explain several unsolved issues in the ADSHE forms caused by hyperfunctional heteromeric nAChRs. First, they suggest that seizures tend to arise during

stages of low cholinergic activity, because cholinergic agonists exert a partial rescue of the local inhibitory deficit in prefrontal circuits and exert a more potent effect on regular spiking SOM+ interneurons. Second, the poor sensitivity to DHβE of the nicotinic currents in RSNP cells points to the expression of non-α4* nAChRs. Because α2* nAChRs are selectively found in layer V Martinotti cells (Hilscher et al., 2017), the simplest interpretation of our results is that, in RSNP cells, β2 mainly participates in α2β2 receptors. The relevance of these observations is founded on increasing evidence about the implication in sleep-related epilepsy of single-site mutations on *CHRNA2*, coding for the α2 nAChR subunit (Aridon et al., 2006; Conti et al., 2015; Villa et al., 2019). The present results point to SOM+ GABAergic neurons as possible culprits of α2-dependent ADSHE.

Finally, our observations may also explain why nicotine is effective as an anti-seizure treatment, in a fraction of ADSHE patients carrying nAChR variants (Becchetti et al., 2020; Fox et al., 2021). Administration of the drug throughout the day could increase the efficacy of surround inhibition in frontal regions, during brain stages characterized by low ACh release.

Author contribution

S.M., A.C. and G.C. carried out and analyzed patch-clamp experiments, D.M., G.C. L.M. and N.M. performed and analyzed immunofluorescence experiments; G.C. carried out Sholl and spine analysis; A.A. and A.B. supervised the work, analyzed the data and wrote the paper; all authors contributed to conceptualization and discussion of the results.

Declarations of interests: none.

References

Amadeo, A., Coatti, A., Aracri, P., Ascagni, M., Iannantuoni, D., Modena, D., Carraresi, L., Brusco, S., Meneghini, S., Arcangeli, A., Becchetti, A., 2018. Postnatal changes in K^+/Cl^- cotransporter-2 expression in the forebrain of mice bearing a mutant nicotinic subunit linked to sleep-related epilepsy. Neuroscience 386, 91-107.

Anastasiades, P.G., Butt, S.J.B., 2012. A role for silent synapses in the development of the pathway from layer 2/3 to 5 pyramidal cells in the neocortex. J. Neurosci. 32:13085-13099.

Aracri, P., Amadeo, A., Pasini, M.E., Fascio, U., Becchetti, A., 2013. Regulation of glutamate release by heteromeric nicotinic receptors in layer V of the secondary motor region (Fr2) in the dorsomedial shoulder of prefrontal cortex in mouse. Synapse 67, 338-357.

Aracri, P., Consonni, S., Morini, R., Perrella, M., Rodighiero, S., Amadeo, A., Becchetti, A., 2010. Tonic modulation of GABA release by nicotinic acetylcholine receptors, in layer V of the murine prefrontal cortex. Cereb. Cortex 20, 1539-1555.

Aracri, P., Banfi, D., Pasini, M.E., Amadeo, A., Becchetti, A., 2015. Orexin (hypocretin) regulates glutamate input to fast-spiking interneurons in layer V of the Fr2 region of the murine prefrontal cortex. Cereb. Cortex 25, 1330-1347.

Aracri, P., Meneghini, S., Coatti, A., Amadeo, A., Becchetti, A., 2017. A4β2* nicotinic receptors stimulate GABA release onto fast-spiking cells in layer V of mouse prefrontal (Fr2) cortex. Neuroscience 340, 48-61.

Aridon, P., Marini, C., Di Resta, C., Brilli, E., De Fusco, M., Politi, F., Parrini, E., Manfredi, I., Pisano, T., Pruna, D., Curia, G., Cianchetti, C., Pasqualetti, M., Becchetti, A., Guerrini, R., Casari, G., 2006. Increased sensitivity of the neuronal nicotinic receptor α2 subunit causes familial epilepsy with nocturnal wandering and ictal fear. Am. J. Hum. Genet. 79, 342-350.

Bailey, C.D., De Biasi, M., Fletcher, P.J., Lambe, E.K., 2010. The nicotinic acetylcholine receptor α5 subunit plays a key role in attention circuitry and accuracy. J. Neurosci. 30, 9241-9252.

Bailey, C.D., Alves, N.C., Nashmi, R., De Biasi, M., Lambe, E.K., 2012. Nicotinic α5 subunits drive developmental changes in the activation and morphology of prefrontal cortex layer VI neurons. Biol. Psychiatry 71, 120-128.

Ballestreros-Yanez, I., Benavides-Piccione, R., Bourgeois, J.P., Changeux, J.P., DeFelipe, J., 2010. Alterations of cortical pyramidal neurons in mice lacking high-affinity nicotinic receptors. Proc. Natl. Acad. Sci. USA 107, 11567-11572.

Barthas, F., Kwan, A.C., 2017. Secondary motor cortex: where 'sensory' meets 'motor' in the rodent frontal cortex. Trends Neurosci. 40, 181-193.

Bean, J.C., Lin, T.W., Sathyamurthy, A., Liu, F., Yin, D.-M., Xiong, W.-C., Mei, L., 2014. Genetic labeling reveals novel cellular targets of schizophrenia susceptibility gene: distribution of GABA and non-GABA ErbB4-positive cells in adult mouse brain. J. Neurosci. 34, 13549-13566.

Becchetti, A., Aracri, P., Meneghini, S., Brusco, S., Amadeo, A., 2015. The role of nicotinic acetylcholine receptors in autosomal dominant nocturnal frontal lobe epilepsy. Front. Physiol. 6, 22.

Becchetti, A., Grandi, L.C., Colombo, G., Meneghini, S., Amadeo, A., 2020. Nicotinic receptors in sleep-related hypermotor epilepsy: pathophysiology and pharmacology. Brain Sci. 10, 907.

Billups, B., Forsythe, I.D., 2002. Presynaptic mitochondrial calcium sequestration influences transmission at mammalian central synapses. J. Neurosci. 22, 5840-5847.

Bolte, S., Cordelières, F.P., 2006. A guided tour into subcellular colocalization analysis in light microscopy. J. Microscopy 224, 213-232.

Braitenberg, V., Schütz, A., 1998. Cortex: Statistics and Geometry of Neuronal Connections, second ed. Springer-Verlag, Berlin.

Bruel-Jungerman, E., Lucassen, P.J., Francis, F., 2011. Cholinergic influences on cortical development and adult neurogenesis. Behav. Brain Res. 221, 379-388.

Cammarota, M., Losi, G., Chiavegato, A., Zonta, M., Carmignoto, G., 2013. Fast spiking interneuron control of seizure propagation in a cortical slice model of focal epilepsy. J. Physiol. 591, 807-822.

Charvet, C.J., Cahalane, D.J., Finlay, B.L., 2015. Systematic, cross-cortex variation in neuron numbers in rodents and primates. Cereb. Cortex 25, 147-160.

Chavez-Noriega, L.E., Crona, J.H., Washburn, M.S., Urrutia, A., Elliott, K.J., Johnson, E.C., 1997. Pharmacological characterization of recombinant human neuronal nicotinic acetylcholine receptors hα2β2, hα2β4, hα3β2, hα3β4, hα4β2, hα4β4 and hα7 expressed in *Xenopus* oocytes. J. Pharmacol. Exp. Ther. 280, 346-356.

Conti, V., Aracri, P., Chiti, L., Brusco, S., Mari, F., Marini, C., Albanese, M., Marchi, A., Liguori, C., Placidi, F., Romigi, A., Becchetti, A., Guerrini, R., 2015. Nocturnal frontal lobe epilepsy with paroxysmal arousals due to CHRNA2 loss of function. Neurology 84, 1520-1528.

Couey, J.J., Meredith, R.M., Spijker, S., Poorthuis, R.B., Smit, A.B., Brussaard, A.B., Mansvelder, H.D., 2007. Distributed network actions by nicotine increase the threshold for spike-timing dependent plasticity in prefrontal cortex. Neuron 54, 73-87.

Dani, J.A., Bertrand, D., 2007. Nicotinic acetylcholine receptors and nicotinic cholinergic mechanisms of the central nervous system. Annu. Rev. Pharmacol. Toxicol. 47, 699-729.

David G., Barrett, E.F., 2003. Mitochondrial Ca^{2+} uptake prevents desynchronization of quantal release and minimizes depletion during repetitive stimulation of mouse motor nerve terminals. J. Physiol. 548, 425-438.

De Fusco, M., Becchetti, A., Patrignani, A., Annesi, G., Gambardella, A., Quattrone, A., Ballabio, A., Wanke, E., Casari, G., 2000. The nicotinic receptor beta 2 subunit is mutant in nocturnal frontal lobe epilepsy. Nat. Genet. 26, 275-276.

Dickinson, J.A., Kew, J.N.C., Wonnacott, S., 2008. Presynaptic α7- and β-containing nicotinic acetylcholine receptors modulate excitatory amino acid release from rat prefrontal cortex nerve terminals via distinct cellular mechanisms. Mol. Pharmacol. 74, 348-359.

Esclapez, M., Houser, C.R., 1999. Up-regulation of GAD65 and GAD67 in remaining hippocampal GABA neurons in a model of temporal lobe epilepsy. J. Comp. Neurol. 412, 488-505.

Fazzari, P., Paternain, A.V., Valiente, M., Pla, R., Luján, R., Lloyd, K., Lerma, J., Marín, O., Rico, B., 2010. Control of cortical GABA circuitry development by Nrg1 and ErbB4 signalling. Nature 464, 1376-1382.

Fenster, C.P., Rains, M.F., Noerager, B., Quick, M.V., Lester, R.A.J., 1997. Influence on subunit composition on desensitization of neuronal acetylcholine receptors at low concentrations of nicotine. J. Neurosci. 17, 5747-5759.

Fonck, C., Cohen, B.N., Nashmi, R., Whiteaker, P., Wagenaar, D.A., Rodrigues-Pinguet, N., Deshpande, P., McKinney, S., Kwoh, S., Munoz, J., Labarca, C., Collins, A.C., Marks, M.J., Lester, H.A., 2005. Novel seizure phenotype and sleep disruptions in knock-in mice with hypersensitive alpha 4* nicotinic receptors. J. Neurosci. 25, 11396-11411.

Fox, J., Thodeson, D.M., Dolce, A.M., 2021. Nicotine: a targeted therapy for epilepsy due to nAChR gene variants. J. Child Neurol. 36, 371-377.

Franklin, K.B.J., Paxinos, G., 2008. The Mouse Brain in Stereotaxic Coordinates, third ed. Elsevier Academic Press, San Diego.

Fukuyama, K., Fukuzawa, M., Shiroyama, T., Okada, M., 2020. Pathogenesis and pathophysiology of autosomal dominant sleep-related hypermotor epilepsy with S284L-mutant α4 subunit of nicotinic ACh receptor. Br. J. Pharmacol. 177, 2143-2162.

Funk, C.M., Peelman, K., Bellesi, M., Marshall, W., Cirelli, C., Tononi, G., 2017. Role of somatostatin-positive cortical interneurons in the generation of sleep slow waves. J. Neurosci. 37, 9132-9148.

Gibbs, S.A., Proserpio, P., Francione, S., Mai, R., Cardinale, F., Sartori, I., Castana, L., Plazzi, G., Tinuper, P., Cossu, M., Lo Russo, G., Tassi, L., Nobili, L., 2018. Clinical features of sleep-related hypermotor epilepsy in relation to the seizure-onset zone: a review of 135 surgically treated cases. Epilepsia 60, 707-717.

Guillem, K., Bloem, B., Poorthuis, R.B., Loos, M., Smit, A.B., Maskos, U., Spijker, S., Mansvelder, H.D., 2011. Nicotinic acetylcholine receptor β2 subunits in the medial prefrontal cortex control attention. Science 333, 888-891.

Gutnick, M.J., Connors, B.W., Prince, D.A., 1982. Mechanisms of neocortical epileptogenesis in vitro. J. Neurophysiol. 48, 1321-1335.

Henny, P., Jones, B.E., 2008. Projections from basal forebrain to prefrontal cortex comprise cholinergic, GABAergic and glutamatergic inputs to pyramidal cells or interneurons. Eur. J. Neurosci. 27, 654-670.

Hilscher, M.M., Leão, R.N., Edwards, S.J., Leão, K.E., Kullander, K., 2017. Chrna2-Martinotti cells synchronize layer 5 type A pyramidal cells via rebound excitation. PLoS Biol. 15, e2001392.

Hioki, H., 2015. Compartmental organization of synaptic inputs to parvalbumin-expressing GABAergic neurons in mouse primary somatosensory cortex. Anat. Sci. Int. 90, 7-21.

Ichikawa, M., Arissian, K., Asanuma, H., 1985. Distribution of corticocortical and thalamocortical synapses on identified motor cortical neurons in the cat: Golgi, electron microscopic and degeneration study. Brain Res. 345, 87-101.

Indurthi, D.C., Qudah, T., Liao, V.W., Ahring, P.K., Lewis, T.M., Balle, T., Chebib, M., Absalom, N.L., 2019. Revisiting autosomal dominant nocturnal frontal lobe epilepsy (ADNFLE) mutations in the nicotinic acetylcholine receptor reveal an increase in efficacy regardless of stoichiometry. Pharmacol. Res. 139, 215-227.

Jones, B.E., 2020. Arousal and sleep circuits. Neuropsychopharmacology 45, 6-20.

Jung, Y., Hsieh, L.S., Lee, A.M., Zhou, Z., Coman, D., Heath, C.J., Hyder, F., Mineur, Y.S., Yuan, Q., Goldman, D., Bordey, A., Picciotto, M.R., 2016. An epigenetic mechanism

mediates developmental nicotine effects on neuronal structure and behavior. Nat. Neurosci. 19, 905-914.

Kameda, H., Hioki, H., Tanaka, Y.H., Tanaka, T., Sohn, J., Sonomura, T., Furuta, T., Fujiyama, F., Kaneko, T., 2012. Parvalbumin-producing cortical interneurons receive inhibitory inputs on proximal portions and cortical excitatory inputs on distal dendrites. Eur. J. Neurosci. 35, 838-854.

Kang, L., Tian, M.K., Bailey, C.D.C., Lambe, E.K., 2015. Dendritic spine density of prefrontal layer 6 pyramidal neurons in relation to apical dendrite sculpting by nicotinic acetylcholine receptors. Front. Cell. Neurosci. 9, 398.

Kasthuri, N., Hayworth, K.J., Berger, D.R., Schalek, R.L., Conchello, J.A., Knowles-Barley, S., Lee, D., Vázquez-Reina, A., Kaynig, V., Jones, T.R., Roberts, M., Morgan, J.L., Tapia, J.C., Seung, H.S., Roncal, W.G., Vogelstein, J.T., Burns, R., Sussman, D.L., Priebe, C.E., Pfister, H., Lichtman, J.W., 2015. Saturated reconstruction of a volume of neocortex. Cell 162, 648-661.

Kawaguchi, Y., 2017. Pyramidal cell subtypes and their synaptic connections in layer 5 of rat frontal cortex. Cereb. Cortex 27, 5755-5771.

Klaassen, A., Glykys, J., Maguire, J., Mody, I., Boulter, J., 2006. Seizures and enhanced cortical GABAergic inhibition in two mouse models of human autosomal dominant nocturnal frontal lobe epilepsy. Proc. Natl. Acad. Sci. USA 103, 19152-19157.

Koch, C., 1999. Biophysics of Computation. Oxford University Press, New York.

Krivosheya, D., Tapia, L., Levinson, J.N., Huang, K., Kang, Y., Hines, R., Ting, A.K., Craig, A.M., Mei, L., Bamji, S.X., El-Husseini, A., 2008. ErbB4-neuregulin signaling modulates synapse development and dendritic arborization through distinct mechanisms. J. Biol. Chem. 283, 32944-32956.

Lawson, J.A., Cook, M.J., Vogrin, S., Litewka, L., Strong, D., Bleasel, A.F., Bye, A.M., 2002. Clinical, EEG, and quantitative MRI differences in pediatric frontal and temporal lobe epilepsy. Neurology 58, 723-729.

Lin, H., Hsu, F.C., Baumann, B.H., Coulter, D.A., Lynch, D.R., 2014. Cortical synaptic NMDA receptor deficits in α7 nicotinic acetylcholine receptor gene deletion models: implications for neuropsychiatric diseases. Neurobiol. Dis. 63, 129-140.

Lozada, A.F., Wang, X., Gounko, N.V., Massey, K.A., Duan, J., Liu, Z., Berg, D.K., 2012. Induction of dendritic spines by β2-containing nicotinic receptors. J. Neurosci. 32, 8391-8400.

Manfredi, I., Zani, A.D., Rampoldi, L., Pegorini, S., Bernascone, I., Moretti, M., Gotti, C., Croci, L., Consalez, G.G., Ferini-Strambi, L., Sala, M., Pattini, L., Casari, G., 2009. Expression of mutant β2 nicotinic receptors during development is crucial for epileptogenesis. Hum. Mol. Genet. 18, 1075-1088.

McLaughlin, T., Torborg, C.L., Feller, M.B., O'Leary, D.D., 2003. Retinotopic map refinement requires spontaneous retinal waves during a brief critical period of development. Neuron 40, 1147-1160.

Metherate, R., Cox, C.L., Ashe, J.H., 1992. Cellular bases of neocortical activation: modulation of neural oscillations by the nucleus basalis and endogenous acetylcholine. J. Neurosci. 12, 4701-4711.

Molas, S., Dierssen, M., 2014. The role of nicotinic receptors in shaping and functioning of the glutamatergic system: a window into cognitive pathology. Neurosci. Biobehav. Rev. 46, 315-325.

Molnár, G., Oláh, S., Komlósi, G., Füle, M., Szabadics, J., Varga, C., Barzó, P., Tamás, G., 2008. Complex events initiated by individual spikes in the human cerebral cortex. PLoS Biol. 6(9), e222.

Moroni, R.F., Deleo, F., Regondi, M.C., Madaschi, L., Amadeo, A., Frassoni, C., 2018. Proliferative cells in the rat developing neocortical grey matter: new insights into gliogenesis. Brain Struct. Funct. 223, 4053-4066.

Müller, T., Braud, S., Jüttner, R., Voigt, B.C., Paulick, K., Sheean, M.E., Klisch, C., Gueneykaya, D., Rathjen, F.G., Geiger, J.R.P., Poulet, J.F.A., Birchmeier, C., 2018. Neuregulin 3 promotes excitatory synapse formation on hippocampal interneurons. EMBO J. 37, e98858.

Nichols, W.A., Henderson, B.J., Marotta, C.B., Yu, C.Y., Richards, C., Dougherty, D.A., Lester, H.A., Cohen, B.N., 2016. Mutation linked to autosomal dominant nocturnal frontal lobe epilepsy reduces low-sensitivity α4β2, and increases α5α4β2, nicotinic receptor surface expression. PLoS One 11, e0158032.

Nigro, M.J., Hashikawa-Yamasaki, Y., Rudy, B., 2018. Diversity and connectivity of layer 5 somatostatin-expressing interneurons in the mouse barrel cortex. J. Neurosci. 38, 1622-1633.

O'Neill, H.C., Laverty, D.C., Patzlaff, N.E., Cohen, B.N., Fonck, C., McKinney, S., McIntosh, J.M., Lindstrom, J.M., Lester, H.A., Grady, S.R., Marks, M.J., 2013. Mice expressing the ADNFLE valine 287 leucine mutation of the β2 nicotinic acetylcholine receptor

subunit display increased sensitivity to acute nicotine administration and altered presynaptic nicotinic receptor function. Pharmacol. Biochem. Behav. 103, 603-621.

Parikh, V., Ji, J., Decker, M.W., Sarter, M., 2010. Prefrontal β2 subunit-containing and α7 nicotinic acetylcholine receptors differentially control glutamatergic and cholinergic signaling. J. Neurosci. 30, 3518-3530.

Parrish, R.R., Codadu, N.K., Mackenzie-Gray Scott, C.A., Trevelyan, A.J., 2019. Feedforward inhibition ahead of ictal wavefronts is provided by both parvalbumin- and somatostatin-expressing interneurons. J. Physiol. 597, 2297-2314.

Phillips, H.A., Favre, I., Kirkpatrick, M., Zuberi, S.M., Goudie, D., Heron, S.E., Scheffer, I.E., Sutherland, G.R., Berkovic, S.F., Bertrand, D., Mulley, J.C., 2001. CHRNB2 is the second acetylcholine receptor subunit associated with autosomal dominant nocturnal frontal lobe epilepsy. Am. J. Hum. Genet. 68, 225-231.

Picciotto, M.R., Highley, M.J., Mineur, Y.S., 2012. Acetylcholine as a neuromodulator: cholinergic signaling shape nervous system function and behavior. Neuron 76, 116-129.

Povysheva, N.V., Gonzalez-Burgos, G., Zaitsev, A.V., Kröner, S., Barrionuevo, G., Lewis, D.A., Krimer, L.S., 2006. Properties of excitatory synaptic responses in fast-spiking interneurons and pyramidal cells from monkey and rat prefrontal cortex. Cereb. Cortex 16, 541-552.

Rahatli, F.K., Sezer, T., Has, A.C., Agildere, A.M., 2020. Evaluation of cortical thickness and brain volume on 3 Tesla magnetic resonance imaging in children with frontal lobe epilepsy. Neurol. Sci. 41, 825-833.

Rehm, H., Wiedenmann, B., Betz, H., 1986. Molecular characterization of synaptophysin, a major calcium-binding protein of the synaptic vesicle membrane. EMBO J. 5, 535-541.

Rossi, F.M., Pizzorusso, T., Porciatti, V., Marubio, L.M., Maffei, L., Changeux, J.P., 2001. Requirement of the nicotinic acetylcholine receptor β2 subunit for the anatomical and functional development of the visual system. Proc. Natl. Acad. Sci. USA 98, 6453-6458.

Sambri, I., Massa, F., Gullo, F., Meneghini, S., Cassina, L., Patanella, L., Carissimo, A., Iuliano, A., Santorelli, F., Codazzi, F., Grohovaz, F., Bernardi, P., Becchetti, A., Casari, G., 2020. Impaired flickering of the permeability transition pore causes SPG7 spastic paraplegia. EBioMedicine 61, 103050.

Sanchez-Vives, M.V., McCormick, D.A., 2000. Cellular and network mechanisms of rhythmic recurrent activity in neocortex. Nat. Neurosci. 3, 1027-1034.

Sharma, G., Vijayaraghavan, S., 2003. Modulation of presynaptic store calcium induces release of glutamate and postsynaptic firing. Neuron 38, 929-939.

Shiba, Y., Mori, F., Yamada, J., Migita, K., Nikaido, Y., Wakabayashi, K., Kaneko, S., Okada, M., Hirose, S., Ueno, S., 2015. Spontaneous epileptic seizures in transgenic rats harboring a human ADNFLE missense mutation in the β2-subunit of the nicotinic acetylcholine receptor. Neurosci. Res. 100, 46-54.

Sholl, D. A., 1953. Dendritic organization in the neurons of the visual and motor cortices of the cat. J. Anat. 87, 387–406.

Son, C.D., Moss, F.J., Cohen, B.N., Lester, H.A., 2009. Nicotine normalizes intracellular subunit stoichiometry of nicotinic receptors carrying mutations linked to autosomal dominant nocturnal frontal lobe epilepsy. Mol. Pharmacol. 75, 1137-1148.

Steinlein, O.K., Mulley, J.C., Propping, P., Wallace, R.H., Phillips, H.A., Sutherland, G.R., Scheffer, I.E., Berkovic, S.F., 1995. A missense mutation in the neuronal nicotinic acetylcholine receptor alpha 4 subunit is associated with autosomal dominant nocturnal frontal lobe epilepsy. Nat. Genet. 11, 201-203.

Telfeian, A.E., Connors, B.W., 1998. Layer-specific pathways for the horizontal propagation of epileptiform discharges in neocortex. Epilepsia 39, 700-708.

Teper, Y., Whyte, D., Cahir, E., Lester, H.A., Grady, S.R., Marks, M.J., Cohen, B.N., Fonck, C., McClure-Begley, T., McIntosh, J.M., Labarca, C., Lawrence, A., Chen, F., Gantois, I., Davies, P.J., Petrou, S., Murphy, M., Waddington, J., Horne, M.K., Berkovic, S.F., Drago, J., 2007. Nicotine-induced dystonic arousal complex in a mouse line harboring a human autosomal-dominant nocturnal frontal lobe epilepsy mutation. J. Neurosci. 27, 10128-10142.

Ting, A.K., Chen, Y., Wen, L., Dong-Min, Y., Shen, C., Tao, Y., Liu, X., Wen-Cheng, X., Mei, L., 2011. Neuregulin 1 promotes excitatory synapse development and function in GABAergic interneurons. J. Neurosci. 31, 15-25.

Tinuper, P., Bisulli, F., Cross, J.H., Hesdorffer, D., Kahane, P., Nobili, L., Provini, F., Scheffer, I.E., Tassi, L., Vignatelli, L., Bassetti, C., Cirignotta, F., Derry, C., Gambardella, A., Guerrini, R., Halasz, P., Lichetta, L., Mahowald, M., Manni, R., Marini, C., Mostacci, B., Naldi, I., Parrino, L., Picard, F., Pugliatti, M., Ryvlin, P., Vigevano, F., Zucconi, M., Berkovic, S., Ottman, R., 2016. Definition and diagnostic criteria of sleep-related hypermotor epilepsy. Neurology 86, 1834-1841.

Tremblay, R., Lee, S., Rudy, B., 2016. GABAergic interneurons in the neocortex: from cellular properties to circuits. Neuron 91, 260-292.

Trevelyan, A.J., Sussillo, D., Watson, B.O., Yuste, R., 2006. Modular propagation of epileptiform activity: evidence for an inhibitory veto in neocortex. J. Neurosci. 26, 12447-12455.

Turrini, P., Casu, M.A., Wong, T.P., De Koninck, Y., Ribeiro-Da-Silva, A., Cuello, A.C., 2001. Cholinergic nerve terminals establish classical synapses in the rat cerebral cortex: synaptic pattern and age-related atrophy. Neuroscience 105, 277-285.

Ueno, S., Bracamontes, J., Zorumski, C., Weiss, D.S., Steinbach. J.H., 1997. Bicuculline and gabazine are allosteric inhibitors of channel opening of the GABA$_A$ receptor. J. Neurosci. 17, 625-634.

van der Kloot, W., Molgó, J., 1994. Quantal acetylcholine release at the vertebrate neuromuscular junction. Physiol. Rev. 74, 899-991.

Villa, C., Colombo, G., Meneghini, S., Moretti, M., Gotti, C., Ferini-Strambi, L., Chisci, E., Giovannoni, R., Becchetti, A., Combi, R., 2019. *CHRNA2* and nocturnal frontal lobe epilepsy: identification and characterization of a novel loss of function mutation. Front. Mol. Neurosci. 12, 17.

Wang, D.D., Kriegstein, A.R., 2008. GABA regulates excitatory synapse formation in the neocortex via NMDA receptor activation. J. Neurosci. 28, 5547-5558.

Widjaja, E., Mahmoodabadi, S.Z., Snead, O.C. 3rd, Almehdar, A., Smith, M.L., 2011. Widespread cortical thinning in children with frontal lobe epilepsy. Epilepsia 52, 1685-1691.

Wong, R.K.S., Traub, R.D., 1983. Synchronized burst discharge in disinhibited hippocampal slice. I. Initiation in CA2-CA3 region. J. Neurophysiol. 49, 442-458.

Xu, J., Cohen, B.N., Zhu, Y., Dziewczapolski, G., Panda, S., Lester, H.A., Heinemann, S.F., Contractor, A., 2011. Altered activity-rest patterns in mice with a human autosomal-dominant nocturnal frontal lobe epilepsy mutation in the β2 nicotinic receptor. Mol. Psychiatry 16, 1048-1061.

Yau, H.-J., Wang, H.-F., Lai, C., Liu, F.-C., 2003. Neural development of the neuregulin receptor ErbB4 in the cerebral cortex and the hippocampus: preferential expression by interneurons tangentially migrating from the ganglionic eminences. Cereb. Cortex 13, 252-264.

Zhou, L., Fisher, M.L., Cole, R.D., Gould, T.J., Parikh, V., Ortinski, P.I., Turner, J.R., 2018. Neuregulin 3 signaling mediates nicotine-dependent synaptic plasticity in the orbitofrontal cortex and cognition. Neuropsychopharmacology 43, 1343-1354.

Zhu, G., Okada, M., Yoshida, S., Ueno, S., Mori, F., Takahara, T., Saito, R., Miura, Y., Kishi, A., Tomiyama, M., Sato, A., Kojima, T., Fukuma, G., Wakabayashi, K., Hase, K., Ohno, H., Kijima, H., Takano, Y., Mitsudome, A., Kaneko, S., Hirose, S., 2008. Rats

harboring S284L *Chrna4* mutation show attenuation of synaptic and extrasynaptic GABAergic transmission and exhibit the nocturnal frontal lobe epilepsy phenotype. J. Neurosci. 28, 12465-12476.

Zwart, R., Vijverberg, H.P., 1997. Potentiation and inhibition of neuronal nicotinic receptors by atropine: competitive and noncompetitive effects. Mol. Pharmacol. 52, 886-895.

FIGURE LEGENDS

Fig. 1. *$\beta2^{V287L}$ did not alter GABAergic cell populations in PFC.*

A, The entire GABAergic population was identified by immunolabeling GAD67 (green). Image is representative of PFC layer V from a Control mouse (P60), with Hoechst counterstaining for nuclei (blue). Calibration bar: 20 μm. **A',** Same as A, for $\beta2^{V287L}$. **B**, Mean GAD67 fluorescence divided by the total number of neurons in PFC layers II/III (PFC II-III) and V (PFC V), for Control and $\beta2^{V287L}$ (P60). Densitometric analysis was carried out on 8 confocal images (4 in layers II/III, and 4 in layer V), for each section. Layers II/III: 0.458 ± 0.049 (Control) and 0.502 ± 0.041 ($\beta2^{V287L}$; NS with unpaired t-test; n = 5 mice per genotype); layer V: 0.405 ± 0.041 (Control) and 0.511 ± 0.040 ($\beta2^{V287L}$; NS with unpaired t-test; n = 5 mice per genotype). **C**, Representative PV cell labeling in PFC (Control, P60). Roman numbers indicate cortex layers. Calibration bar: 125 μm. **D**, Higher magnification in layer V, in a section labeled for PV and counterstained with thionin. Calibration bar: 20 μm. To standardize cell counts, we used dissectors with two green and two red adjacent sides, as displayed. Only the cell bodies in the dissector and those on the green sides were counted. **E**, Mean estimated number of PV+ cells in total PFC (PFC) and PFC layer V (PFC V), for Control and $\beta2^{V287L}$. These estimates cover the entire rostrocaudal extension of PFC (Table 1). PFC: 6533 ± 1058 (Control) and 6982 ± 1125 ($\beta2^{V287L}$; NS with unpaired t-test; n = 5 mice per genotype, P60); PFC V: 5252 ± 829 (Control) and 5258 ± 399 ($\beta2^{V287L}$; NS with unpaired t-test; n = 5 mice per genotype, P60). **F**, Representative confocal microscope images of double immunofluorescence labeling of PV

(blue), in PFC layer V from a Control mouse. Calibration bar: 20 µm. **F',** Same as F, for $\beta2^{V287L}$. **G**, Mean number of PV+ cells in total PFC (PFC) and PFC layer V (PFC V), for Control and $\beta2^{V287L}$. Counting was performed on 4 sampled confocal image stacks (total thickness 6 µm) for each section and for each area. PFC: 95 ± 8 (Control) and 112 ± 20 ($\beta2^{V287L}$; NS with unpaired t-test; n = 3 mice per genotype, P90); PFC V: 58 ± 5 (Control) and 75 ± 14 ($\beta2^{V287L}$; NS with unpaired t-test; n = 3 mice per genotype, P90). **H**, Same as F, for SOM (red), in the same section. Calibration bar: 20 µm. **H',** Same as H, for $\beta2^{V287L}$. **I**, Same as G, for SOM+ cells. PFC: 117 ± 9 (Control) and 124 ± 13 ($\beta2^{V287L}$; NS with unpaired t-test; n = 3 mice per genotype, P90); PFC V: 72 ± 3 (Control) and 71 ± 7 ($\beta2^{V287L}$; NS with unpaired t-test; n = 3 mice per genotype, P90).

Fig. 2. *$\beta2^{V287L}$ did not alter cholinergic innervation*

A, Representative ChAT labeling in PPT and LDT. Calibration bar: 20 µm. **A',** Same as A, for $\beta2^{V287L}$. **B**, Same as A, for NBM. Calibration bar: 20 µm. **B',** Same as B, for $\beta2^{V287L}$. **C**, Mean estimated number of ChAT+ cells in LDT, PPT and NBM. LDT: 4372 ± 402 (Control, n = 5) and 5418 ± 763 ($\beta2^{V287L}$, n = 6; NS with unpaired t-test); PPT: 4691 ± 1090 (Control, n = 5) and 4725 ± 429 ($\beta2^{V287L}$, n = 6; NS with unpaired t-test); NBM: 519 ± 34 (Control) and 770 ± 158 ($\beta2^{V287L}$; NS with unpaired t-test, n = 6 mice per genotype). **D**, Typical ChAT labeling in PFC (Control). Roman numbers indicate cortex layers. Calibration bar: 100 µm. **E**, Same as D, at higher magnification of layer V. Calibration bar: 25 µm. **F**, ChAT densitometric values were used to evaluate the cholinergic fibers in PFC. In layer II/III (PFC II/III), the mean optical density was 0.127 ± 0.014 (Control), and 0.139 ± 0.009 ($\beta2^{V287L}$; NS with unpaired t-test; n = 5 mice per genotype). In layer V (PFC V), the mean optical density was 0.124 ± 0.012 (Control) and 0.136 ± 0.009 ($\beta2^{V287L}$; NS with unpaired t-test; n = 5 mice per genotype). **G**, Confocal image stack (total thickness 6 µm) of VAChT immunofluorescent labeling (green), showing typical cholinergic innervation in PFC layer V, in a Control mouse. Calibration bar: 20 µm. G',

Same as G, for $\beta2^{V287L}$. **H**, Mean VAChT fluorescence in total PFC (PFC) and V layer (PFC V), for Control and $\beta2^{V287L}$, as indicated. Densitometric analysis was carried out on 24 confocal images (from four different 6 μm thick stacks) for each section and for each area. PFC: 48.1 ± 1.62 (Control) and 45.37 ± 1.49 ($\beta2^{V287L}$; NS with unpaired t-test; n = 3 mice per genotype, P90); PFC V: 47.52 ± 1.9 (Control) and 45.67 ± 1.31 ($\beta2^{V287L}$; NS with unpaired t-test; n = 3 mice per genotype, P90). **I,** Representative confocal image stacks (total thickness 22 μm) from sections with double immunolabeling of VAChT (green) combined with PV (blue) in PFC layer V of a Control mouse. Calibration bars: 20 μm. **J**, Same as I, for SOM cells (red). **K**, Average number of VAChT+ contacting terminals divided by the total number of PV+ and SOM+ cells in PFC layer V of Control mice. VAChT/PV: 59 ± 8 (n = 81 cells; 3 Control mice); VAChT/SOM 51 ± 6 (n = 60 cells; 3 Control mice; NS with unpaired t-test).

Fig. 3. *Characterization of RSNP SOM+ neurons in Fr2 layer V.*

A, Representative 3D image reconstructed from a section with triple immunolabeling of VAChT (green), SOM (red) and PV (light blue) in PFC layer V of a Control mouse. The confocal microscope z-stack was 10.5 μm thick (63×, zoom 2). Notice that the numerosity of PV+ and SOM+ cells was comparable in layer V. Calibration bar: 10 μm. **B**, Post-recording 3D reconstruction of an RSNP cell loaded with neurobiotin and identified by Alexa-488-streptavidin labeling (10.8 μm z-stack, 40×). Calibration bar: 10 μm. **C**, Post-recording reconstruction of a SOM+ RSNP neuron, merged channels (max projection of a 10.4 μm z-stack, 60×). **C'**, DAPI labeling to identify the nucleus (the neuron shape is outlined). **C''**, biocytin labeling (green). **C'''**, SOM labeling (red). Calibration bar: 10 μm. **D**, Firing pattern of the cell illustrated in B. Stimulus was 200 pA for 500 ms. **E**, Average stimulus-frequency relation from a representative group of RSNP neurons from age-matched (P50-P60) mice: Control (black; n = 6), $\beta2^{V287L}$ (white, n = 4). The indicated stimuli were applied for 500 ms.

No statistical difference was observed between genotypes. **E**, Focal application of 5-HT onto the RSNP cell body caused no appreciable whole-cell current response (V_m = -68 mV).

Fig. 4. *Spontaneous EPSCs and IPSCs in pyramidal, FS and RSNP cells, in mice expressing or not $\beta2^{V287L}$.*

A, Representative EPSC recordings from a Control (tTA) and a $\beta2^{V287L}$ pyramidal neuron. Top panels show action potential firing (200 pA stimulus). Bottom panels show the respective spontaneous EPSCs (at two different time scales) during continuous recording at -70 mV. **B**, Representative IPSC traces from a Control (tTA) and a $\beta2^{V287L}$ pyramidal neuron. Spontaneous IPSCs were recorded as outward current events at +10 mV and displayed at two different time scales. **C**, Spontaneous EPSC frequencies registered from the indicated cell types and genotypes, during the 4th, 5th, 6th week and >P42. No significant difference was found between the EPSC frequencies measured in different weeks from the same cell type and genotype. For example, in Control (tTA) FS cells, EPSC frequencies were 40.1 ± 3.2 Hz (5th week, n = 7), and 40.8 ± 3.4 Hz (6th week, n =5), 36 ± 3.4 Hz (>P42, n = 7; NS with one-way ANOVA). In $\beta2^{V287L}$, EPSC frequency was 25.3 ± 2.9 Hz (5th week; n = 12), 21 ± 2.1 Hz (6th week, n = 17), 27 ± 0.3 Hz (>P42; n = 3; NS with one-way ANOVA). Spontaneous EPSC frequencies were generally lower in RSNP cells. For instance, in the 5th week EPSC frequency was 3.1 ± 0.84 in Control (n = 8) and 3.3 ± 0.48 in $\beta2^{V287L}$ (n = 9; NS with unpaired t-test). These values remained stable up to the 4th month (>90). **D**, Representative EPSCs recordings from a Control (tTA) and a $\beta2^{V287L}$ FS neuron. Top panels show AP firing (200 pA stimulus). Bottom panels show the respective spontaneous EPSCs (at two different time scales) during continuous recording at -70 mV. **E**, Average spontaneous EPSC or IPSC frequency in pyramidal, FS and RSNP cells, in Control or $\beta2^{V287L}$, between the 5th week and P60. EPSCs in pyramidal cells: Control, 15 ± 2.2 Hz (n = 12); $\beta2^{V287L}$, 14.3 ± 2.9 Hz (n = 9; NS with unpaired t-test); EPSCs in FS cells: Control,

38.8 ± 1.9 Hz (n = 19); $\beta2^{V287L}$, 23.1 ± 1.6 Hz (n = 31); Control + doxycycline, 33.92 ± 1.8 Hz (n = 7); $\beta2^{V287L}$ + doxycycline, 35.2 ± 2.1 Hz (n = 7). One-way ANOVA: p = 7.7E-8 (Control and $\beta2^{V287L}$); p = 0.015 (Control + doxycycline and $\beta2^{V287L}$); p = 0.005 ($\beta2^{V287L}$ and $\beta2^{V287L}$ + doxycycline); the other comparisons were NS. EPSCs in RSNP cells: Control, 2.8 ± 0.41 Hz (n = 38); $\beta2^{V287L}$, 2.94 ± 0.44 Hz (n = 15; NS with unpaired t-test). IPSCs in pyramidal cells: Control, 8.5 ± 1.42 Hz (n = 15); $\beta2^{V287L}$, 6.5 ± 1.2 Hz (n = 23; p = 0.04 with Mann-Whitney test; medians were, respectively 7.23 Hz and 4.7 Hz); IPSCs in FS cells: Control, 8.56 ± 4 Hz (n = 5); $\beta2^{V287L}$, 8.57 ± 3.4 Hz (n = 9; NS with Mann-Whitney test). IPSCs in RSNP cells: Control, 17.8 ± 4.5 Hz (n = 7); $\beta2^{V287L}$, 17.3 ± 3.8 Hz (n = 6; NS with unpaired t-test).

Fig. 5. *$\beta2^{V287L}$ decreased the mEPSC frequency in FS neurons.*

A, Spontaneous EPSC traces for a Control (tTA) FS neuron, in absence and presence of TTX, at -70 mV. Cell firing (with 200 pA stimulus) is shown on the top panel. **B**, Same as A, for a $\beta2^{V287L}$ FS neuron. **C**, Distribution of interevent intervals (left) and events' amplitudes (right), for the experiment shown in A, in presence or absence of TTX. As expected, TTX decreased both events' frequency and amplitude. Data are representative of 10 experiments. **D**, Same as C, for the $\beta2^{V287L}$ FS neuron shown in B. Data are representative of 19 experiments. **E**, Average frequency of mEPSCs in Control (19.9 ± 2.45 Hz, n = 10) and $\beta2^{V287L}$ (9.94 ± 1.60 Hz, n = 19; p = 0.0016 with unpaired t-test). **F**, Averages of the median mEPSC amplitudes: 7.6 ± 0.54 Hz (Control, n = 10) and 8.7 ± 0.54 Hz ($\beta2^{V287L}$, n = 19; NS with unpaired t-test).

Fig. 6. *Effect of $\beta2^{V287L}$ on the distribution of excitatory synapses on PV+ and SOM+ cells.*

A, Representative 3D image reconstructed from a section with double immunolabeling of VGLUT1 and PV (**A'**). VGLUT1+ terminals were automatically segmented while PV+ cells were drawn manually using ArivisVision4D software. Calibration bar: 10 μm. **A'**, Inset is representative of PFC layer V from a Control P90 mouse, acquired at 63×, zoom 2. Calibration

bar: 10 μm. **B**, Average number of VGLUT1+ terminals per PV+ cell, in PFC layer V of Control and $\beta2^{V287L}$. Control: 60 ± 4.65 (n = 63 cells; 3 mice); $\beta2^{V287L}$: 84.67 ± 2.17 (n = 72 cells; 3 mice; p = 0.0086 with unpaired t-test). **C**, Distribution of VGLUT1+ terminals among layer V PV+ cells. for 3 Control mice. Bin size is 10, i.e. each bin represents the number of cells displaying 0 to 10, or 11 to 20, etc. terminals. **D**, Same as C, for $\beta2^{V287L}$. **E**, Same as A, for VGLUT1 and SOM immunolabeling. **E'**, Inset is representative of PFC layer V from a Control P90 mouse, acquired at 63×, zoom 2. Calibration bar: 10 μm. **F**, Average number of VGLUT1+ terminals per SOM+ cell, in PFC layer V of Control and $\beta2^{V287L}$. Control: 54.55 ± 4.78 (n = 91 cells; 3 mice); $\beta2^{V287L}$: 53.33 ± 3.72 (n = 78 cells; 3 mice; NS with unpaired t-test). **G**, Distribution of VGLUT1+ terminals in layer V SOM+ cells, for 3 Control mice. Bin size is as in C. **H**. Same as G, for $\beta2^{V287L}$.

Fig. 7. *Effect of $\beta2^{V287L}$ on the distribution of inhibitory synapses on PV+ and SOM+ cells.*
A, Representative 3D image reconstructed from a section with double immunolabeling of VGAT and PV, as indicated. Calibration bar: 10 μm. VGAT+ terminals were automatically segmented, while PV+ cells were drawn manually using ArivisVision4D software. **A'**, Inset is representative of PFC layer V from a Control P90 mouse, acquired at 63×, zoom 2. Calibration bar: 10 μm. **B**, Average number of VGAT+ terminals per PV+ cell, in PFC layer V of Control and $\beta2^{V287L}$. Control: 188.29 ± 5.45 (n = 64 cells; 3 mice); $\beta2^{V287L}$ 190.96 ± 7.88 (n = 63 cells; 3 mice; NS with unpaired t-test). **C**, Distribution of VGAT+ terminals among layer V PV+ cells of 3 Control mice. Bin size is as in Fig. 5. **D**, Same as C, for $\beta2^{V287L}$. **E**, Same as A, for VGAT and SOM immunolabeling. **E'**, Inset is representative of PFC layer V from a Control P90 mouse, acquired at 63×, zoom 2. Calibration bar: 10 μm. **F**, Average number of VGAT+ terminals per SOM+ cells, in PFC layer V of Control and $\beta2^{V287L}$. Control: 152.71 ± 20.13 (n = 66 cells; 3 mice); $\beta2^{V287L}$: 132.6 ± 6.25 (n = 62 cells; 3 mice; NS with unpaired t-test). **G**,

Distribution of VGAT+ terminals in layer V SOM+ cells for 3 Control mice. Bin size is as in C. **H**, Same as G, for $\beta2^{V287L}$.

Fig. 8. *Effect of nAChR stimulation on EPSCs and IPSCs in pyramidal and FS neurons.*

A, After testing pyramidal neuron AP firing (left panel), spontaneous EPSCs were recorded at -68 mV, for 5 min in ACSF, 5 min in ACSF + 10 μM nicotine (Nicotine), and 5 min after nicotine was washed out. Right panel: representative current traces for 5 s continuous recording in the indicated conditions. Nicotine increased the EPSC frequency, as the median interevent interval decreased from 86.4 ms (ACSF, n = 839 events) to 72.6 (Nicotine, n = 1140 events; p = 3.7E-5, KS test). **B**, Same as A, for $\beta2^{V287L}$. Nicotine decreased the median interevent interval from 122.3 ms (ACSF, n = 589 events) to 70.7 ms (Nicotine, n = 1034 events; p = 8.6E-14, KS test). **C**, Distribution of the interevent intervals for the Control and $\beta2^{V287L}$ experiments illustrated in A and B, in ACSF or in presence of nicotine, as indicated. **D**, Average effects produced by nicotine on a population of pyramidal neurons. EPSC and IPSC frequencies were calculated from experiments carried out in Control or $\beta2^{V287L}$, as indicated. EPSCs: Control, 13.5 ± 2.56 Hz (ACSF) and 21.1 ± 3.97 (nicotine; p = 4.8E-4, paired t-test, n = 11); $\beta2^{V287L}$, 12.0 ± 2.01 Hz (ACSF) and 22.4 ± 4.59 (nicotine; p = 0.024, paired t-test, n = 9). IPSCs: Control, 6.3 ± 0.91 Hz (ACSF) and 8.2 ± 0.95 (nicotine; p = 0.0028, paired t-test, n = 9); $\beta2^{V287L}$, 3.8 ± 0.90 Hz (ACSF) and 6.5 ± 0.85 (nicotine; p = 8.4E-4, paired t-test, n = 9). **E**, Same as A, for a Control FS neuron. The median interevent interval decreased from 18 ms (ACSF; n = 5619 events) to 16.8 ms (nicotine, n = 6454 events; p = 6E-14 with KS test). **F**, Same as E, for $\beta2^{V287L}$. The median interevent interval decreased from 20.4 ms (ACSF; n = 4017 events) to 16.7 ms (nicotine, n = 6494 events; p = 1.7E-64 with KS test). **G**, Cumulative probability of the interevent intervals for the Control and $\beta2^{V287L}$ experiments illustrated in E and F, in ACSF or in presence of nicotine, as indicated. **H**, Same as D, for EPSCs recorded on FS neurons: Control, 39.9 ± 4.7 Hz (ACSF) and 48.6 ± 4.9 (nicotine; p = 0.01, paired t-test, n = 9); $\beta2^{V287L}$, 19.77 ±

2.67 Hz (ACSF) and 30.8 ± 4.9 (nicotine; p = 0.0063, paired t-test, n = 9). **I**, Percentage increase produced by nicotine on synaptic event frequency, in the indicated conditions. IPSCs in pyramidal neurons (median values): Control 28%, $\beta 2^{V287L}$ 67% (p = 0.03; Mann-Whitney test). EPSCs in FS neurons (median values): Control 15%, $\beta 2^{V287L}$ 39% (p = 0.026; Mann-Whitney test). **J**, Average of the median EPSC amplitudes recorded on pyramidal neurons. Control, 10.5 ± 0.83 pA (ACSF) and 11.2 ± 1.09 pA (nicotine; NS with paired t-test, n = 9); $\beta 2^{V287L}$ 9.2 ± 0.31 pA (ACSF) and 10.3 ± 1.04 pA (nicotine; NS with paired t-test, n = 9). **K**, Averages of the median EPSC amplitudes recorded on FS cells. Control, 11.2 ± 0.94 pA (ACSF) and 12.9 ± 1.16 pA (nicotine; NS with paired t-test, n = 9); $\beta 2^{V287L}$, 10.9 ± 1.2 pA (ACSF) and 12.6 ± 2.7 pA (nicotine; NS with paired t-test, n = 9).

Fig. 9. *Somatic nicotinic currents in RSNP SOM+ cells.*

A, Left panel: firing profile of a representative Control RSNP neuron. Right panel: continuous whole-cell recording at -70 mV, in presence and absence of nicotine (10 μM). Continuous line indicates the time of nicotine application. **B**, Same as A, for $\beta 2^{V287L}$. **C**, Left panel: average peak whole-cell currents elicited by 10 μM nicotine in RSNP cells of the indicated genotype. Control, 14.7 ± 1.85 pA (n = 14); $\beta 2^{V287L}$, 26.9 ± 4.9 pA/pF (n = 12; p = 0.035, unpaired t-test). The respective peak current densities are reported in the right panel: Control, 0.386 ± 0.04 pA/pF (n = 14); $\beta 2^{V287L}$, 0.687 ± 0.12 pA/pF (n = 12; p = 0.027, with unpaired t-test). **D**, Same as A, but nicotine was applied in the presence of DHβE (1 μM). Continuous lines indicate the time of DHβE application, and the time during which nicotine (10 μM) was added to DHβE, as indicated. DHβE was unable to block nAChR currents. **E**, Same as D, but in presence of 30 μM DHβE. This concentration of DHβE fully blocked the somatic current activated by 10 μM nicotine. **F**, Average peak current densities elicited by 10 μM nicotine, in the presence of 1 μM DHβE (5.0 ± 0.74 pA/pF; n = 7), and 30 μM DHβE (0.81 ± 0.22 pA/pF; n = 10; p < 0.0001, unpaired t-test).

Fig. 10. *Excitability of pyramidal neurons expressing or not β2^{V287L}.*

A, Representative continuous V_m recording in a pyramidal neuron from a WT, in the following conditions: ACSF, ACSF + 2 μM bicuculline (Bicuculline), ACSF + 2 μM bicuculline + 10 μM nicotine (Bicuculline + Nicotine). The cell's V_{rest} was approximately -67 mV. ACSF was applied for 2 min, Bicuculline for 5 min and Bicuculline + Nicotine for 5 min. Notice the spike events observed in Bicuculline + Nicotine. **B**, Expansion of the area framed by the gray box on A, to highlight the spike events. **C**, Same as A, for tTA. **D**, Same as A, for β2^{V287L}. **E**, Frequency of EPSP events larger than 2 mV (EPSP$_{2mV}$) recorded for 2 min in ACSF from Control (tTA + WT) and β2^{V287L}. Bars give the median number of EPSP$_{2mV}$ per min: Control, 0.8 min^{-1} (n = 13); β2^{V287L}, 1.6 min^{-1} (n = 9; p = 0.0095 with Mann-Whitney t-test) **F**, Percentage of slices displaying AP burst activity in Control (tTA + WT) and β2^{V287L}, in presence in Bicuculline or Nicotine, at the indicated concentration of bicuculline.

Supplementary Fig. 1. *Effect of β2^{V287L} on PFC thickness and layer V neuronal population*

A, Thionin PFC staining was used to analyse cortical thickness and cell count. Roman numbers indicate cortical layers, in PFC of a Control (P60). Calibration bar: 100 μm. **B**, Average PFC thickness in Control and β2^{V287L}, at the indicated postnatal ages. A significant decrease was observed since P12 in β2^{V287L}. P9: 1349.3 ± 40.4 μm (Control) and 1293.7 ± 41.4 μm (β2^{V287L}; NS with unpaired t-test; n = 5 mice per genotype); P12: 1418.4 ± 20.1 μm (Control) and 1311.5 ± 19.2 μm (β2^{V287L}, p = 0.0085 with t-test; n = 4 mice per genotype); P60: 1437.1 ± 24.3 μm (Control) and 1294.9 ± 41.9 μm (β2^{V287L}, p = 0.0189 with t-test; n = 5 mice per genotype); P120: 1421.9 ± 3.0 μm (Control) and 1318.8 ± 14.98 μm (β2^{V287L}, p = 0.0016 with t-test; n = 4 mice per genotype). For comparison, the corresponding values in SS at P60 were: Control: 1300 ± 49 μm, β2^{V287L}: 1310 ± 57 μm (NS with unpaired t-test; n = 5 mice per genotype). **C**, As in A, but at a higher magnification to highlight layer V. Neurons were counted by stereology using

the displayed dissector (as explained in Fig. 1). Calibration bar: 25 μm. **D,** Representative image at a lower magnification from PFC layer V of a Control mouse. Calibration bar: 50 μm. **D',** same as D, for $\beta2^{V287L}$. **E,** Average neuronal counts in PFC layer V of Control and $\beta2^{V287L}$ (P60): Control, 25667 ± 2000; $\beta2^{V287L}$, 22730 ± 2136 (NS with unpaired t-test; n = 5 mice per genotype). For comparison, in SS we estimated 61250 ± 3190 neurons in Control and 58000 ± 4255 in $\beta2^{V287L}$ (NS with unpaired t-test; n = 5 mice per genotype). The higher cell count in SS is consistent with previous observations in mammals (e.g., Charvet et al., 2015).

Supplementary Fig. 2. *$\beta2^{V287L}$ did not alter overall glutamatergic innervation in PFC.*

A, Typical VGLUT1 immunolabeling in PFC layer V from a Control mouse (P90). Glutamatergic terminals were broadly distributed around negative neuronal cell bodies. Calibration bar: 50 μm. **A',** same as A, for $\beta2^{V287L}$. **B,** VGLUT1 densitometric values were used to quantify intrinsic glutamatergic input in PFC. In layer II-III (PFC II/III), the mean optical density was 0.242 ± 0.013 (Control) and 0.218 ± 0.011 ($\beta2^{V287L}$; NS with unpaired t-test; n = 9 mice per genotype). In layer V (PFC V), the mean optical density was 0.232 ± 0.010 (Control) and 0.198 ± 0.012 ($\beta2^{V287L}$; NS with unpaired t-test; n = 9 mice per genotype).

Supplementary Fig. 3. *Spine density and dendrite complexity in pyramidal neurons.*

A, Spine density in layers II/III pyramidal neurons. Data points give the number of spines counted within 10 μm dendrite segments, up to 110 μm from soma, in Control (white circles) and $\beta2^{V287L}$ (black circles). No significant differences were observed between genotypes. For instance (at 10 μm): Control, 6.38 ± 0.69 (n = 4 mice); $\beta2^{V287L}$, 5.97 ± 0.79 (n = 4 mice; NS with unpaired t-test). At 20 μm: Control, 7.38 ± 1.6 (n = 4 mice); $\beta2^{V287L}$, 7.59 ± 1.08 (n = 4 mice; NS with unpaired t-test). **B,** Same as A, for layer V pyramidal neurons. The results obtained with Control and $\beta2^{V287L}$ were not statistically different. For instance (at 10 μm): Control, 3.62 ± 0.96 (n = 4 mice); $\beta2^{V287L}$, 5.05 ± 1.46 (n = 4 mice; NS with unpaired t-test).

At 20 μm: Control, 6.28 ± 0.71 (n = 4 mice); β2^{V287L}, 6.41 ± 0.77 (n = 4 mice; NS with unpaired t-test). **C**, Dendrite complexity in layer V pyramidal neurons for Control and β2^{V287L}. Data points represent the number of intersections with dendrites within spherical shells at increasing distance from the soma. Inset gives the Schoenen ramification index for Control (2.75 ± 0.15, n = 4 mice) and β2^{V287L} (2.12 ± 0.22, n = 4 mice; NS with unpaired t-test).

Supplementary Fig. 4. *β2^{V287L} did not alter GABA$_A$R and β2* nAChR expressions in PFC*

A, GABA$_A$R expression was identified by immunolabeling of the α1 GABA$_A$R subunit (green) counterstained with NeuroTrace^{TM} (red; NT). Image is representative of PFC layer V from a Control mouse; GABA$_A$R+ structures comprise neuronal cell bodies and neuropil. A' Same as A, for β2^{V287L}. **B,** Mean GABA$_A$R fluorescence divided by the total number of neurons in PFC layers II/III (PFC II-III) and V (PFC V), for Control and β2^{V287L}. Layers II/III: 0.712 ± 0.117 (Control) and 0.825 ± 0.129 (β2^{V287L}; NS with unpaired t-test; n = 5 mice per genotype); layer V: 0.595 ± 0.088 (Control) and 0.546 ± 0.063 (β2^{V287L}; NS with unpaired t-test; n = 5 mice per genotype). **C,** Confocal microscope image of β2 nAChR subunit immunolabeling (red) in PFC layer V from a Control mouse (P60), with Hoechst counterstaining for nuclei (blue). C', Same as C, for β2^{V287L}. **D**, Data are mean fluorescence values divided by the number of neurons. Layers II/III: 0.638 ± 0.045 (Control) and 0.572 ± 0.030 (β2^{V287L}; NS with unpaired t-test; n = 3 mice per genotype); layer V: 0.607 ± 0.077 (Control) and 0.442 ± 0.039 (β2^{V287L}; NS with unpaired t-test; n = 3 mice per genotype). **E**, Representative image of colocalization of β2 nAChR subunit (green) and SYN (red), in PFC layer V from a β2^{V287L} mouse (P60). **F,** 2D cytofluorogram selecting the colocalization puncta (white dots in **E**) in the region of interest (enclosed by the yellow ellipsoid) for the β2/SYN immunolabeling showed in **E,** hence indicating β2* nAChR presynaptic expression. **G**, Colocalization analysis between β2 nAChR subunit and SYN. Bars represent the Manders' coefficient 1 (M1) indicating the amount of β2* nAChR expressed in PFC synaptic terminals. Layers II/III: 0.787 ± 0.011 (Control) and 0.746

± 0.070 ($\beta2^{V287L}$; NS with unpaired t-test; n = 3 mice per genotype); layer V: 0.692 ± 0.039 (Control) and 0.641 ± 0.091 ($\beta2^{V287L}$; NS with unpaired t-test; n = 3 mice per genotype). Calibration bars: 20 μm.

Table 1. *Parameters used for section choice and stereological counts.*

Area	Neurons	Distance from bregma (mm)	Grid (μm)	Counting frame/dissector (μm)
PFC	PV+	+2.58, +2.18, +1.54, +1.14, +0.74, +0.34, -0.06	80 x 80	80 x 80
SS	PV+	+1.54, +0.74, -0.06, -0.86, -1.64	80 x 80	80 x 80
NBM	ChAT+	-0.34, -0.50, - 0.82	100 x 100	80 x 80
LDT PPT	ChAT+	-5.02, -4.96, -4.84, -4.72, -4.60, -4.48, -4.36	100 x 100	50 x 50

Table 2. *Expression of $\beta 2^{V287L}$ did not alter V_{rest} and firing of FS and RSNP cells.*

Cell type	V_{rest} (mV)	Spike width (ms)	4th spike interval/ 1st spike interval	AHP (mV)	*N*
FS					
Control	-70.1 ± 0.33	0.84 ± 0.05	1.18 ± 0.04	-13.8 ± 0.96	15
$\beta 2^{V287L}$	-70.8 ± 1.03	0.89 ± 0.05	1.18 ± 0.03	-12.9 ± 1.03	12
RSNP					
Control	-71.3 ± 0.48	1.78 ± 0.09	2.58 ± 0.28	-7.3 ± 0.6	14
$\beta 2^{V287L}$	-72.1 ± 0.57	1.84 ± 0.08	2.51 ± 0.31	-6.3 ± 0.56	14

The indicated electrophysiological parameters were measured in a representative sample of Fr2 slices from Control and $\beta 2^{V287L}$ mice, in their second postnatal month. The ratio between the 4th and the 1st spike interval was calculated under a 200 pA stimulation. No statistical difference was found between Control and $\beta 2^{V287L}$, in any of the measured parameters (unpaired t-test). AHP: after-hyperpolarization.

Figure 1
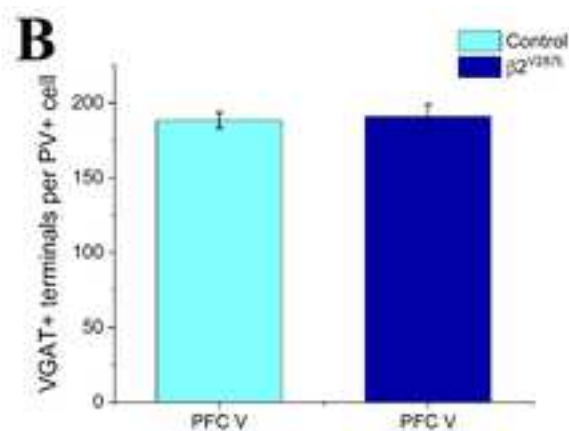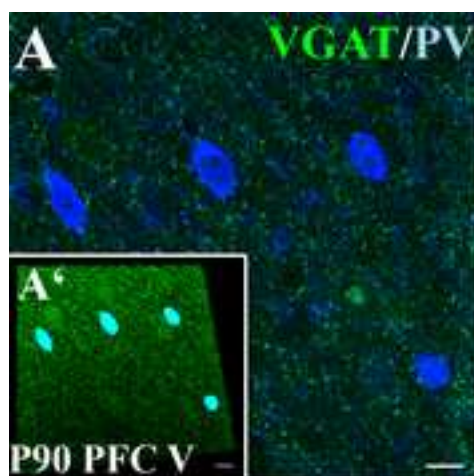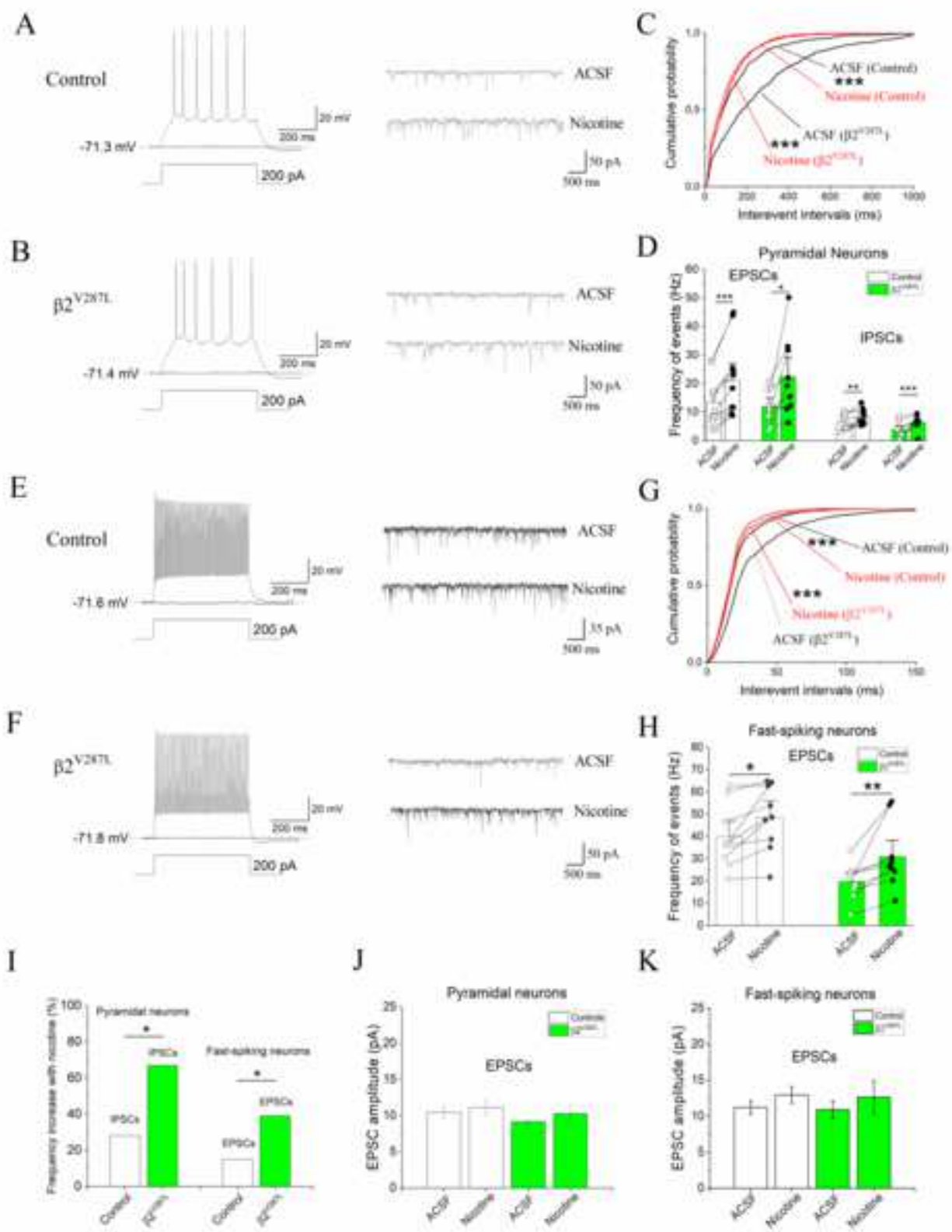
Figure 2

Click here to access/download;Figure;Meneghini Fig. 2 R2.tif
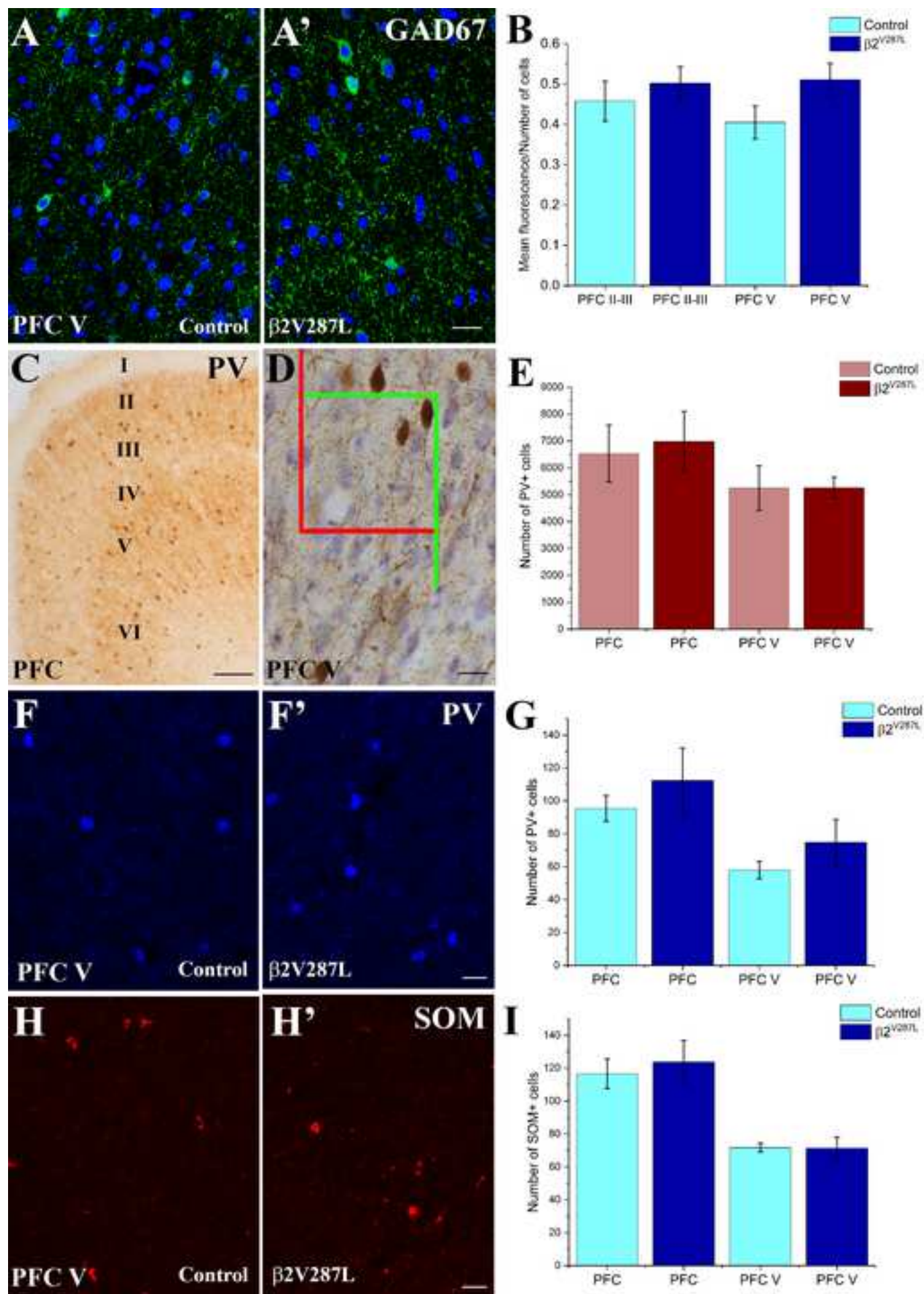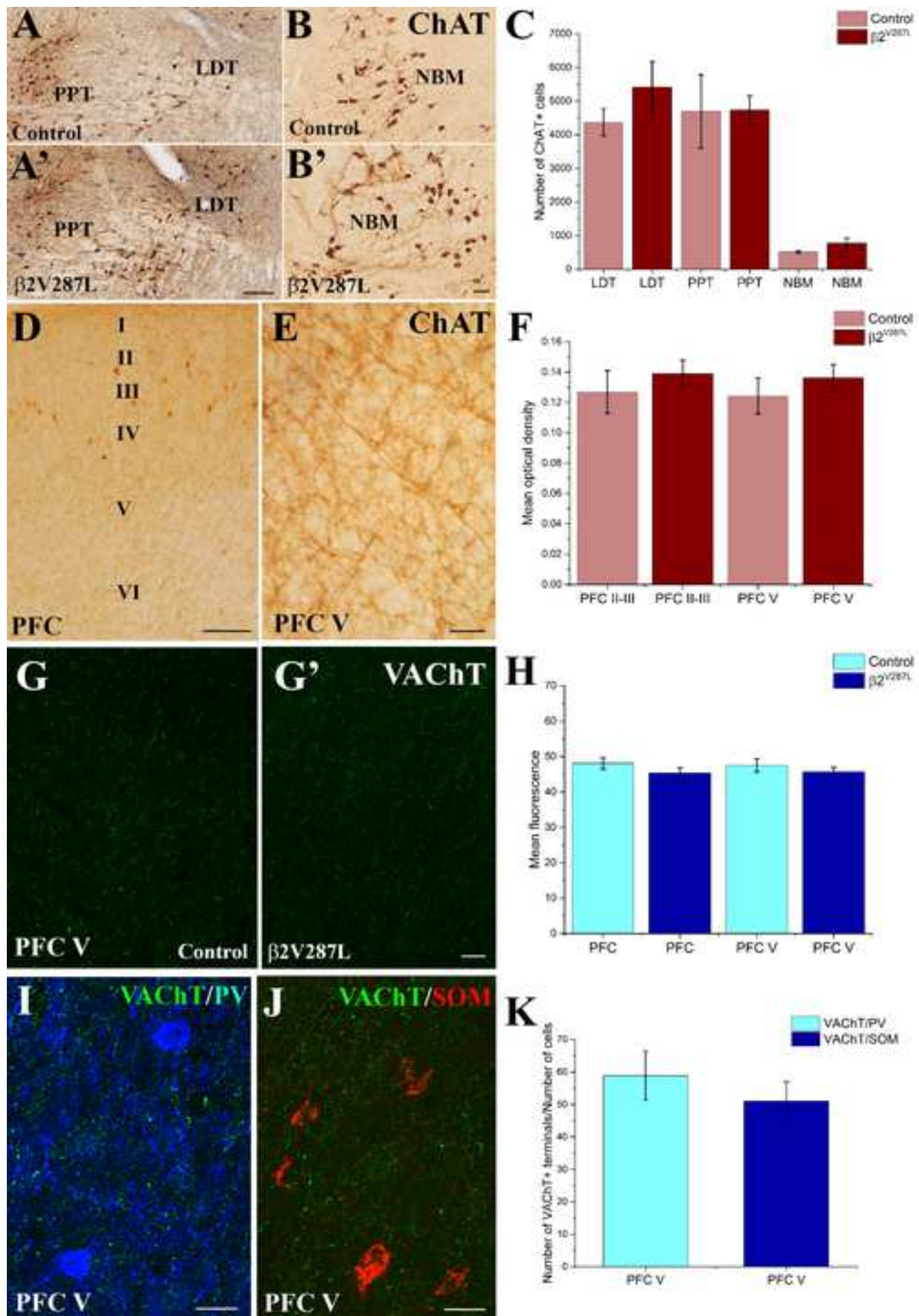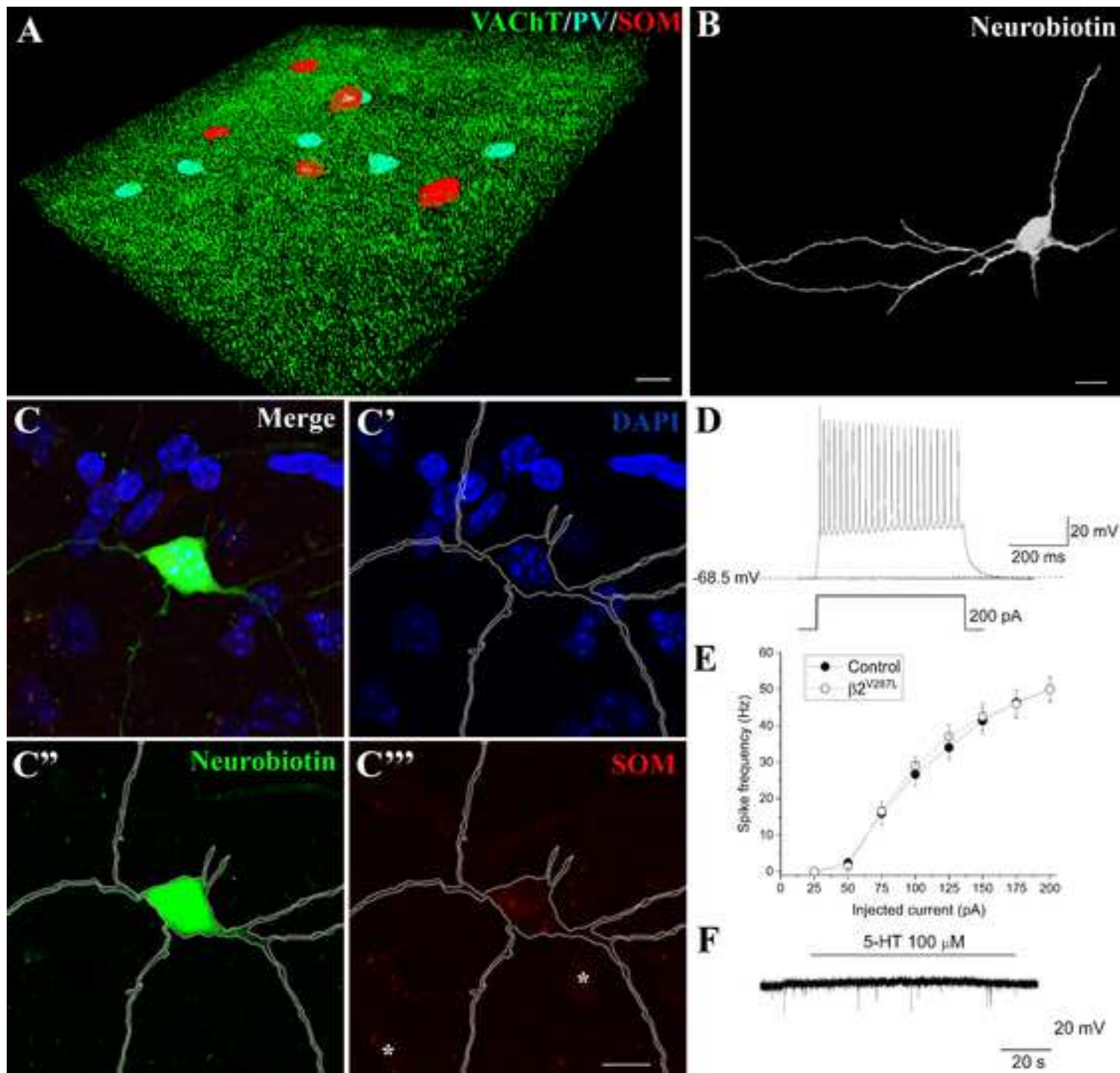
Figure 4

Figure 4
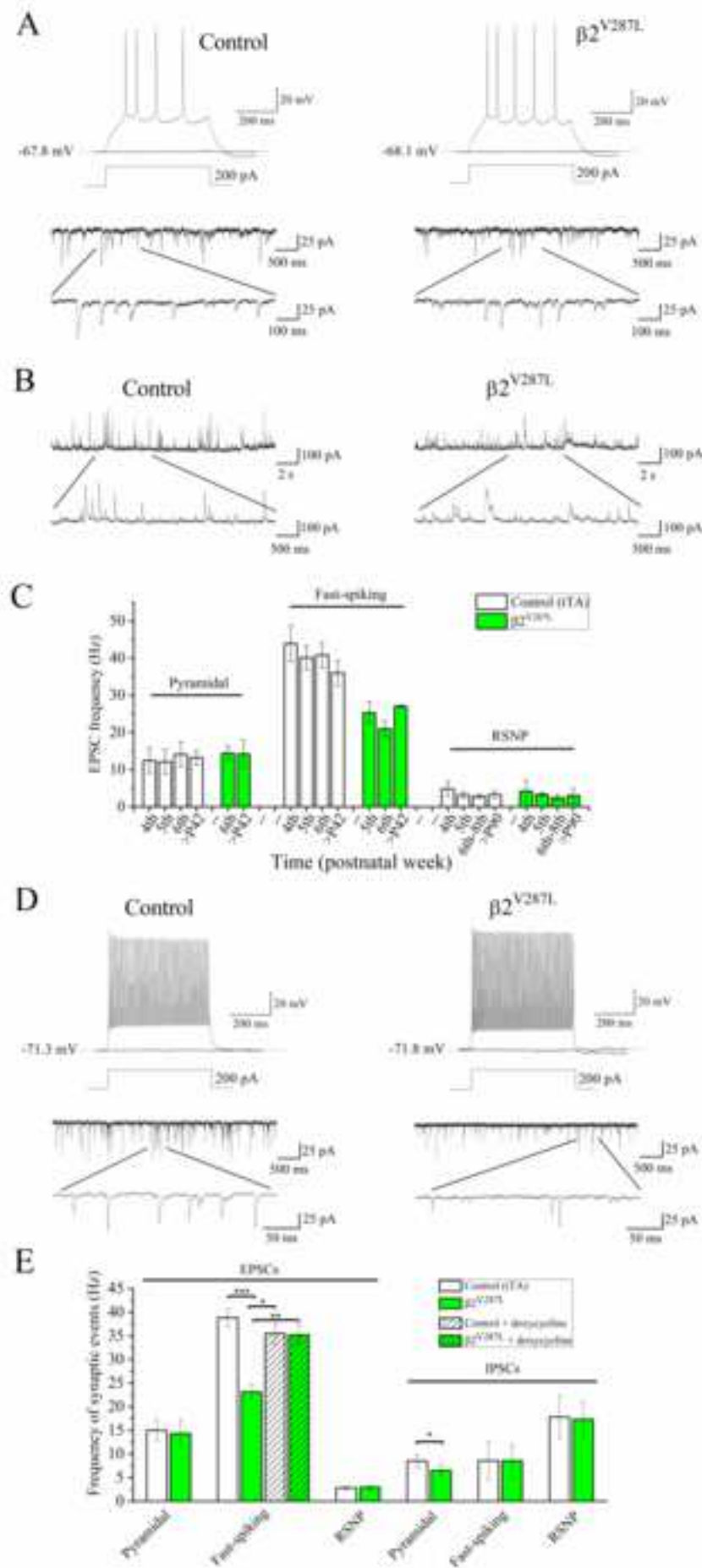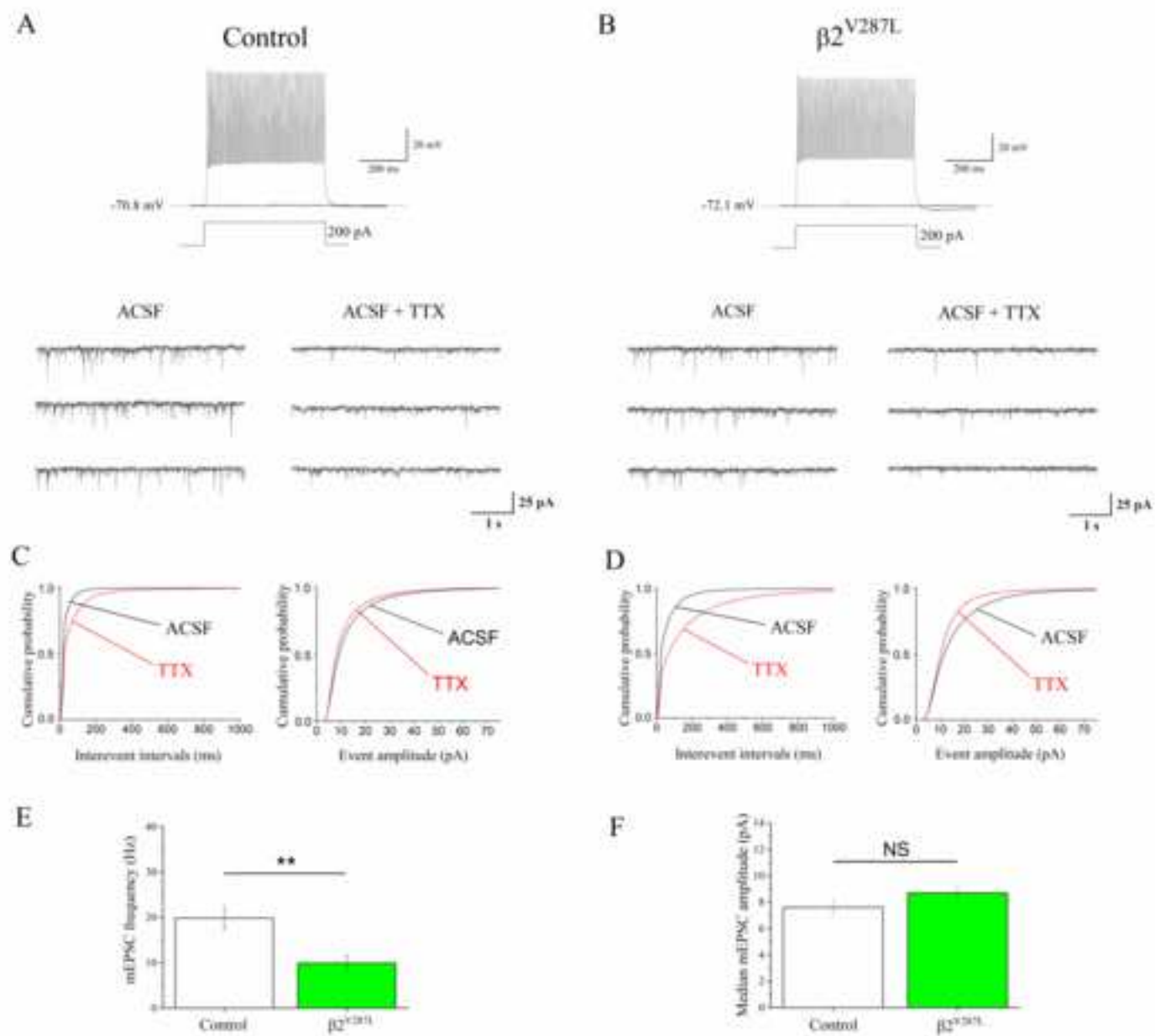
Figure 5
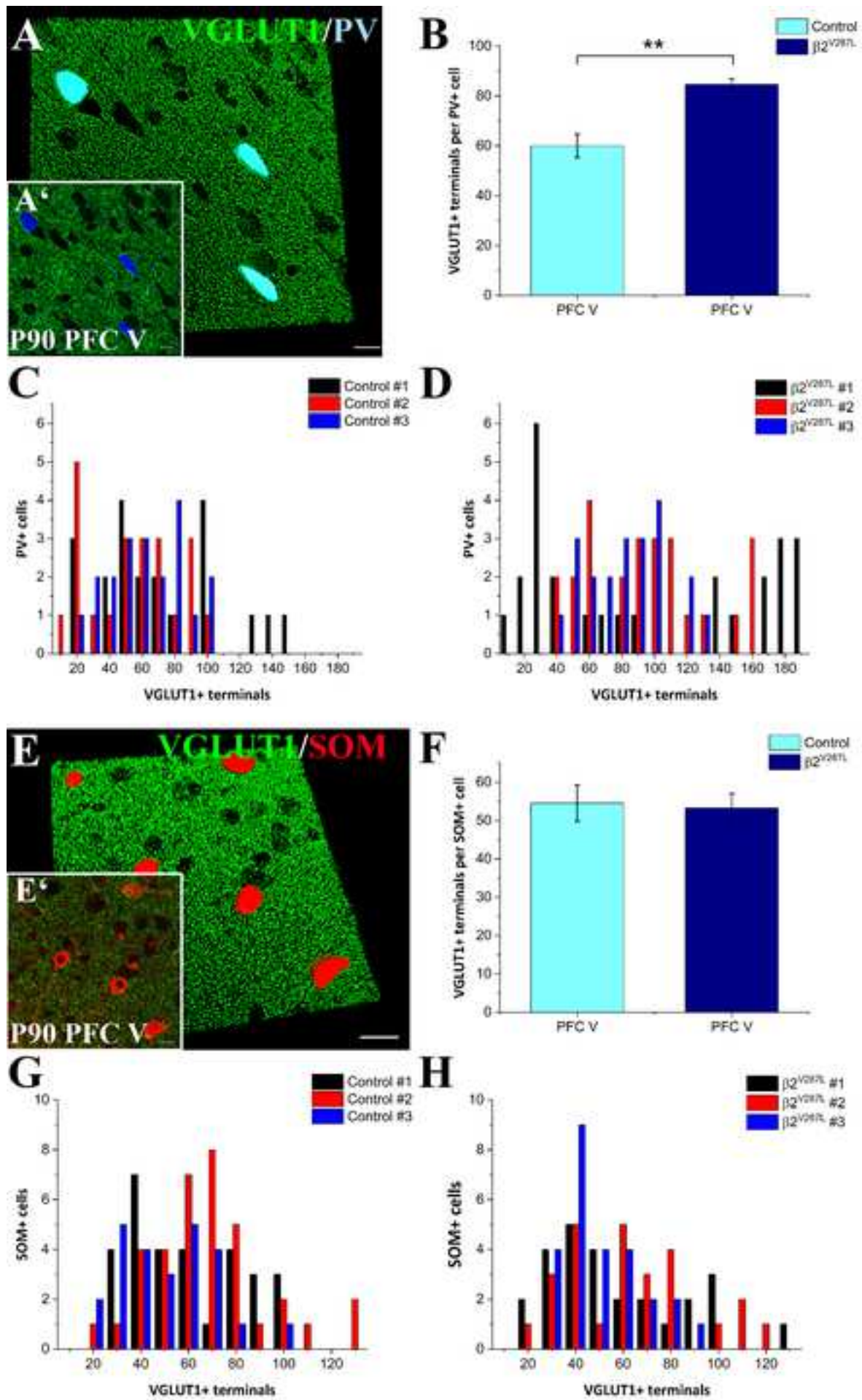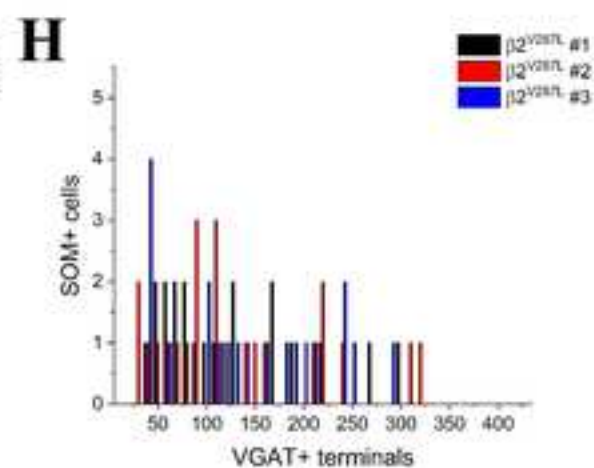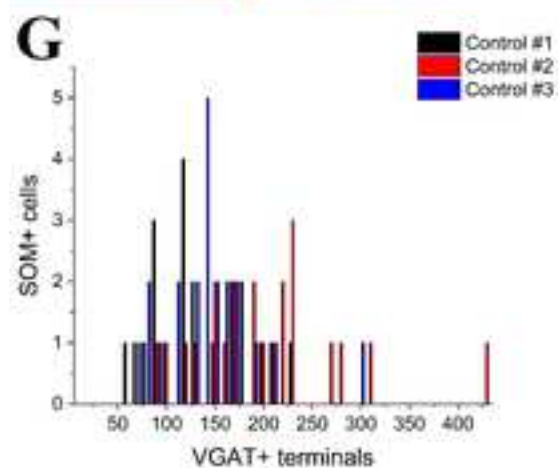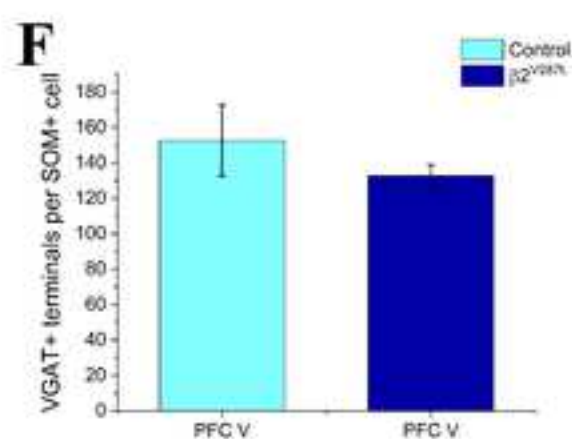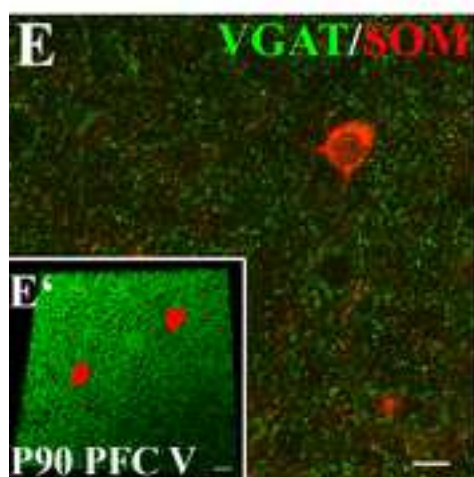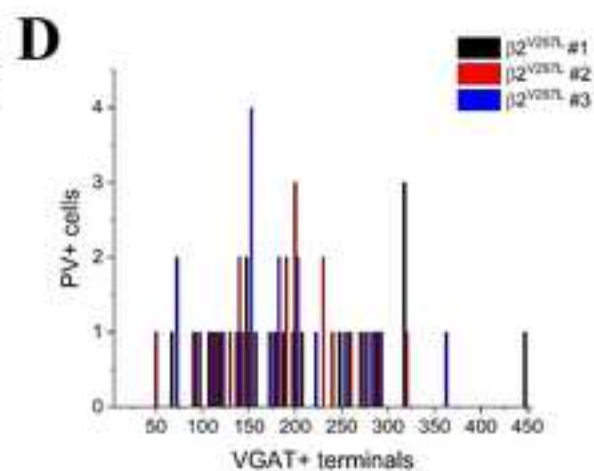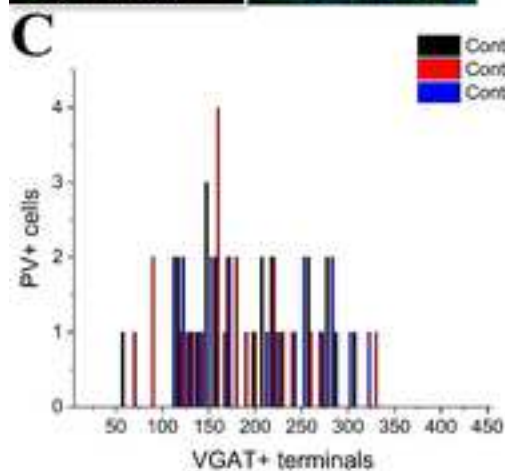
Figure 6

Figure 7

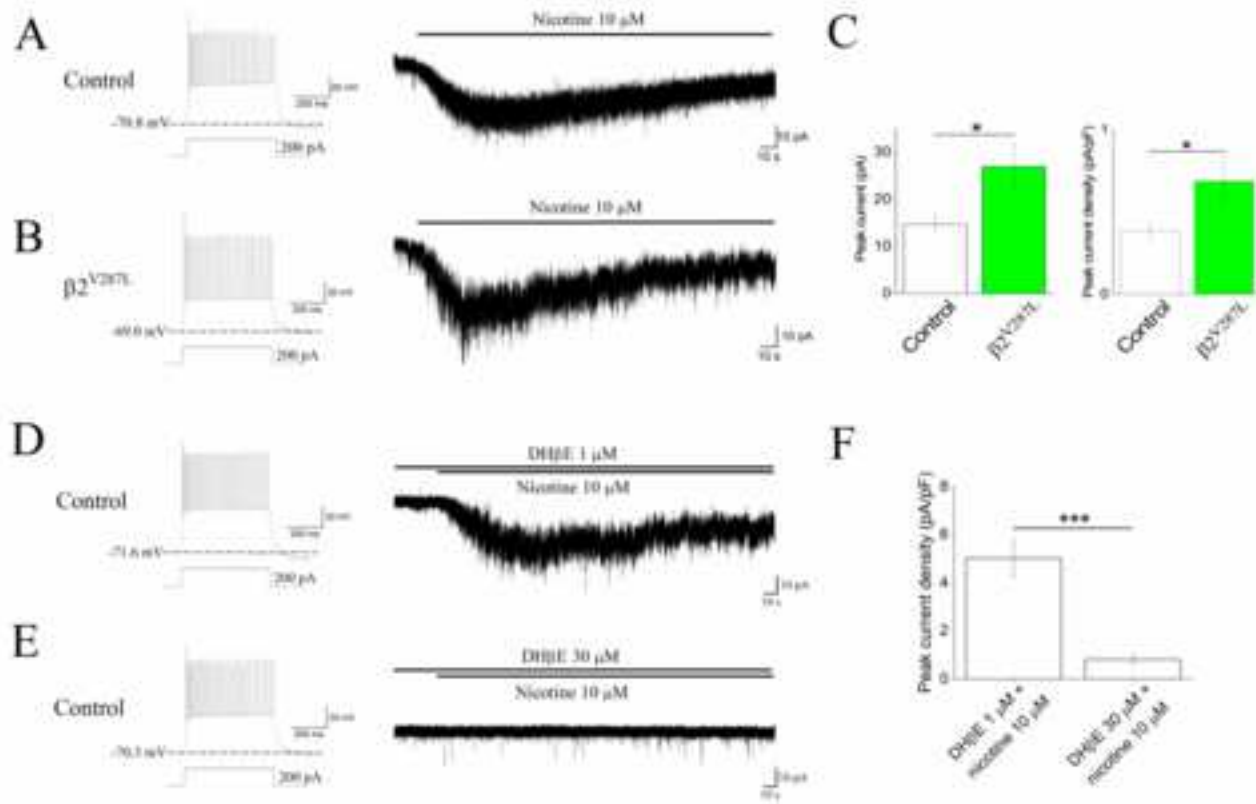**Figure 8**

Figure 9

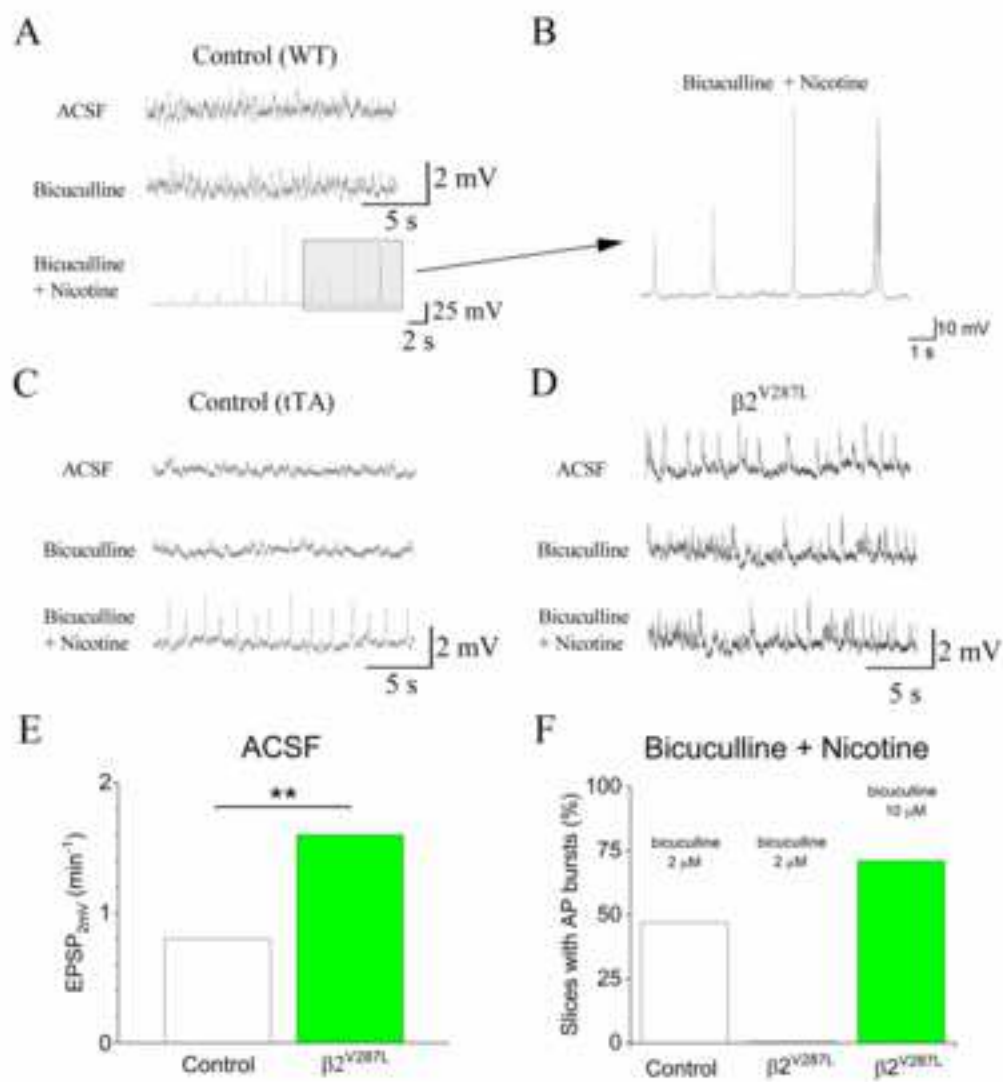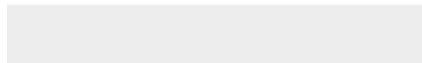**Figure 9**

Figure 9

Supplementary Fig. 1

Click here to access/download
Supplementary Material
Meneghini Suppl Fig. 1 R2.tif

Click here to access/download
Supplementary Material
Meneghini Suppl Fig 3.tif

Click here to access/download

Supplementary Material

Meneghini Suppl Fig. 4 R2.tif